Title	Carbonation of oceanic serpentinite related to extensive intraplate magmatism
Author(s)	Ryosuke Oyanagi, Hikaru Sawada, Qing Chang, Kenta Yoshida, Madhusoodhan Satish-Kumar
Citation	Journal title (Repository name etc.), Volume, Issue, Pages (Article number) etc. ・ジャーナル名（刊行物・サイト名）・巻号・ページ（その他論文番号等）： Geological Society of America Bulletin ・DOI (URL) https://doi.org/10.1130/B38019.1 Publication Date: yyyy/mm/dd ・出版日：2025 年 8 月 29 日 Publisher ・出版者：Geological Society of America
Declaration	This preprint is the Author Accepted Manuscript (AAM) of the above. ・本プレプリントは、上記論文の (受理済) 著者最終稿 (AAM) である。 All necessary permissions from the publisher have been obtained (得ている) ・ジャーナル（出版者）から必要な許諾を
Notes	This is a pre-copyedited, author-produced version of an article accepted for publication in Geological Society of America following peer review. The version of record is available online at https://doi.org/10.1130/B38019.1

Carbonation of oceanic serpentinite related to extensive intraplate magmatism*

Ryosuke Oyanagi†
School of Engineering and Science, Kokushikan University, Tokyo 154-8515, Japan and
Research Institute for Marine Geodynamics (IMG), Japan Agency for
Marine-Earth Science and Technology (JAMSTEC), Yokosuka 237-0061, Japan

Hikaru Sawada
Department of Earth System Science, University of Toyama, Toyama, 930-0887, Japan and
Institute for Extra-cutting-edge Science and Technology Avant-garde Research (X-star),
Japan Agency for Marine-Earth Science and Technology (JAMSTEC), Yokosuka 237-0061, Japan

Qing Chang and Kenta Yoshida
Research Institute for Marine Geodynamics (IMG), Japan Agency for
Marine-Earth Science and Technology (JAMSTEC), Yokosuka 237-0061, Japan

Madhusoodhan Satish-Kumar
Department of Geology, Faculty of Science, Niigata University, Niigata 950-2181, Japan

Extensive intraplate magmatism that forms oceanic plateaux involves significant carbon outflux and perturbation of the global carbon cycle, potentially linking to climate change, oceanic anoxia, and mass extinction events. Hydrothermal alteration related to such magmatism can modify the major element composition of the oceanic lithosphere around the hydrothermal system. However, the relationship between carbon mass transfer and hydrothermal systems associated with intraplate magmatism remains unclear. This study investigated carbonated serpentinites occurring along with mafic meta-volcanic rocks, which were part of an oceanic plateau in the Late Jurassic Paleo-Pacific Ocean. Carbonate minerals (calcite and dolomite) occur as cement in the serpentinite breccias and in discrete veins in the serpentinite. C–O–Sr isotopic compositions and rare earth element data for the carbonates suggest the calcite cements in the serpentinite breccias formed in an oceanic setting by the mixing of seawater and hydrothermal fluids before subduction. The strontium isotopic compositions of the seawater-derived carbonates suggest that carbonation most likely occurred concurrently with the formation of an oceanic plateau, suggesting intraplate magmatism plays an important role as a carbon sink by inducing alteration and carbonation during associated hydrothermal activity. Moreover, our results suggest the calcite and dolomites formed in a subduction zone from CO_2-rich fluids sourced by the devolatilization of metasediments, after the accretion of an oceanic plateau. These results may indicate that the life cycle of oceanic plateaux can cause perturbations in carbon influx and outflux, and that the interplay between oceanic plateau emplacement, subsequent alteration, and carbon uptake may have modulated atmospheric CO_2 and Earth's surface environments.

I. INTRODUCTION

The long-term carbon cycle in Earth's interior has regulated its surface climate and habitability throughout geological history, and is controlled by the balance between carbon influx from, and outflux into, Earth's subsurface (Kelemen and Manning, 2015; Plank and Manning, 2019; Müller et al., 2022). The carbon that is carried into Earth's interior is hosted by subducting sediments, and hydrated oceanic crust and hydrated mantle, and the net carbon influx is estimated to be 82 ± 14 Mt C yr^{-1} (Plank and Manning, 2019). Carbon is returned to Earth's subsurface by volcanism, and the net carbon outflux is estimated to be 79 ± 9 Mt C yr^{-1} (Plank and Manning, 2019). The global carbon influx and outflux are thought to be broadly in balance (Kelemen and Manning, 2015; Plank and Manning, 2019). However, our understanding of the carbon influx and outflux in submarine environments (e.g., mid-ocean ridges and submarine arc volcanoes) is limited, as the large size and inaccessibility of these environments could mean there are unrecognized components of the geological carbon cycle (Burton et al., 2013; Black and Gibson, 2019; Klein et al., 2024).

Large igneous provinces (LIPs) are caused by occasional large mantle-derived fluxes into Earth's subsurface. LIPs form flood basalt provinces in continental settings and oceanic plateaux on oceanic crust in marine settings (Coffin and Eldholm, 1994; Kerr, 2014; Tetreault and Buiter, 2014; Ernst et al., 2021). LIPs formation involves significant carbon outflux over geologically short timescales (10^5-10^6 yr; Black and Gibson, 2019) and the carbon emission rate during such events is estimated to be 4–250 Mt C yr^{-1} (Jiang et al., 2022). Correlations between LIPs, extinction events, and climatic changes suggest that the extensive volcanism related to LIPs may produce perturbations of subsurface environments (Jones et al., 2016). However, the increased atmospheric carbon dioxide and global warming associated with LIPs volcanism can enhance the chemical weathering of silicate rocks, and this re-

---

[*] This is a pre-copyedited, author-produced version of an article accepted for publication in *Geological Society of America Bulletin* following peer review. The version of record is available online at `https://doi.org/10.1130/B38019.1`

[†] Corresponding Author. oyanagir@kokushikan.ac.jp

moves more carbon than that initially injected into the atmosphere on timescales as short as 1 Myr (Dessert et al., 2003; Schaller et al., 2012; Johansson et al., 2018). Therefore, LIPs may cause short-term disturbances of the carbon cycle and surface environments, but may actually be a net carbon sink over longer timescales. Such a negative feedback on the geological carbon cycle has been reported for continental LIPs (Schaller et al., 2012; Johansson et al., 2018), whereas the feedback associated with oceanic LIPs is unclear, given their inaccessibility and the scarcity of samples. The geochemical evolution and subsequent alteration of oceanic plateaux have been mainly inferred rather than measured or observed (Sager et al., 2016). The few geological studies on the hydrothermal alteration of modern oceanic plateaux have proposed that hydrothermal alteration is a result of magmatic activity during formation of the plateau (Li et al., 2014; Beier et al., 2019). In these studies, carbon sequestration in the oceanic plateau was inferred based on carbonate precipitation due to hydrothermal alteration at various temperatures (0–360°C). Our understanding of the hydrothermal alteration during oceanic plateau formation is limited, particularly around the Moho depth, where it is composed of the ultramafic cumulate (Kerr et al., 1998; Ridley and Richards, 2010; Kerr, 2014), which have the potential to sequester significant amounts of carbon (Kelemen and Manning, 2015; Müller et al., 2022; Leong et al., 2023; Menzel et al., 2024; Oyanagi and Okamoto, 2024). Infiltration of seawater and alteration of the mantle rock can be induced by the thermal cracking that occurs during the ascent and eruption of plume lavas (Park and Rye, 2019a, b).

Although drilling to the base of modern oceanic plateaux is challenging, the basal layer of oceanic plateaux (gabbros, pyroxenite, and dunites) can be exposed via thrust faults during plateau accretion and imbrication (Nivia, 1996; Kerr et al., 1998; Tetreault and Buiter, 2012). Therefore, accreted paleo-oceanic plateaux exposed in orogenic belts document important geological processes that occur in modern oceanic plateaux located in submarine settings (Coffin and Eldholm, 1994; Kerr, 2014). The Mikabu unit in southwest Japan is regarded to be an accreted fragment of a Jurassic paleo-oceanic plateau (i.e., the Mikabu Plateau) formed due to a large, hot mantle plume (Isozaki et al., 1990; Kimura et al., 1994; Ichiyama et al., 2014). Ultramafic cumulates associated with oceanic intraplate (plume-related) magmatism occur in the Mikabu unit (Agata, 1994; Uesugi and Arai, 1999; Ichiyama et al., 2014). Thus, the ultramafic cumulates in the Mikabu unit may have multiple geological alteration events from an oceanic to accretionary setting, and provide a unique opportunity to investigate the relationship between extensive intraplate magmatism and hydrothermal alteration during the emplacement of an oceanic plateau.

In this study, we investigated a serpentinite body in the Kanasaki area of the Mikabu unit (Kanasaki serpentinites). The Kanasaki serpentinites contain unique occurrences of carbonate mineral veins that have long been recognized by geologists and utilized as building materials in Tokyo. We examined the petrography of the Kanasaki serpentinites, and used C–O–Sr isotopic and rare earth element (REE) compositions of carbonates from the serpentinites to constrain their fluid source and timing of carbonation. These data are used to discuss the relationship between intraplate magmatism and hydrothermal alteration, as well as their potential influence on global carbon cycling.

II. GEOLOGICAL SETTING

The Sanbagawa metamorphic terrane (including the Mikabu unit) is a Cretaceous, subduction-related intermediate- to high-P–T metamorphic belt that extends for $\sim$ 800 km along the southwestern part of Japan and the median tectonic line (MTL), which is a crustal-scale fault (Fig. 1A; Wallis et al., 2020; Endo et al., 2024). The main part of the Sanbagawa metamorphic terrane contains paraschists (pelitic and psammitic) and mafic schists, along with minor metachert. Blocks of serpentinized mantle rocks are a minor but widespread component (Kunugiza et al., 1986; Banno, 2004; Hattori et al., 2010; Aoya et al., 2013; Mizukami et al., 2014; Hirauchi et al., 2021; Okamoto et al., 2021, 2024; Oyanagi et al., 2023). The peak metamorphic conditions obtained by conventional geothermobarometers and phase equilibria are $\sim$360°C and 0.5–0.6 GPa (pumpellyite–actinolite facies) in the chlorite zone, 425–455°C and 0.7–0.9 GPa (greenschist facies) in the garnet zone, 495–545°C and 0.8–1.0 GPa (epidote amphibolite facies) in the albite–biotite zone, and 585–635°C and 0.9–1.1 GPa (epidote amphibolite facies) in the oligoclase–biotite zone (Enami, 1983; Enami et al., 1994; Wallis et al., 2000). Some of the high-grade rocks in central Shikoku experienced eclogite-facies metamorphism (Wallis and Aoya, 2000; Endo et al., 2009; Kouketsu et al., 2014; Yoshida et al., 2021).

The Mikabu unit is a weakly metamorphosed mafic – ultramafic unit that occurs discontinuously as a narrow belt (¡5 km wide) along the southern part of the Sanbagawa metamorphic terrane (Koto, 1888; Ishiwatari et al., 2016; Wallis et al., 2020). The Mikabu unit has undergone greenschist-facies metamorphism and is part of the Sanbagawa metamorphic terrane in terms of metamorphism. However, the Mikabu unit is tectonically and lithologically distinct from the Sanbagawa metamorphic terrane (Ishiwatari et al., 2016; Wallis et al., 2020). The Mikabu unit is tectonically underlain by the Sanbagawa metamorphic terrane and is overlain by the Chichibu belt, a Jurassic accretionary complex (Makimoto and Takeuchi, 1992). The Mikabu unit is predominantly composed of mafic volcanic rocks (hyaloclastite, pillow and massive lavas, and mafic dikes) with lesser amount of gabbro, serpentinite, and metasedimentary rocks (pelagic chert, terrigenous metapelite, and reef limestone) (Tokuda, 1986; Makimoto and Takeuchi, 1992).

Mafic rocks in the Mikabu unit are picritic, tholeiitic, and alkali basalts in composition (Agata, 1994; Ozawa et al., 1997; Tatsumi et al., 1998; Uesugi and Arai, 1999; Ichiyama et al., 2014), similar to those in oceanic plateaux such as the Ontong Java and Caribbean oceanic plateau (Tejada et al., 2002; Hastie and Kerr, 2010; Kerr, 2014). The trace element compositions of the Mikabu mafic rocks exhibit mid-ocean-ridge-basalt like trace element signatures (Ozawa et al. 1997),

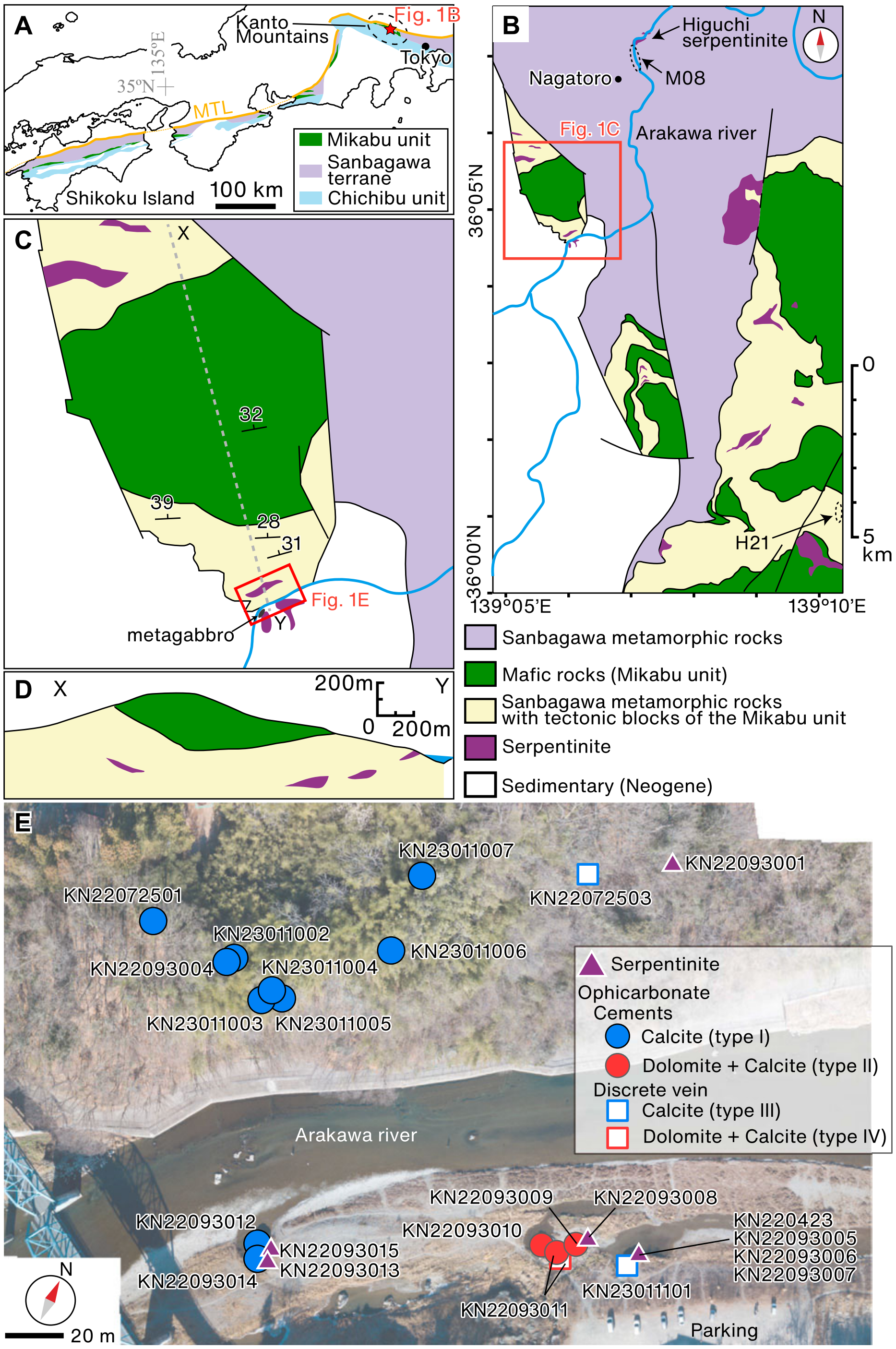

FIG. 1. Distribution of the Mikabu unit and location of the Kanto Mountains (modified from Wallis et al., 2020). The yellow line is the Median Tectonic Line (MTL). (B) Geological map around the area of the red star in Fig. 1A (modified from Makimoto and Takeuchi, 1992). The areas indicated by the dotted black ellipses show the locations of related studies; M08 = Morohashi et al., 2008); H21 = Hara et al. (2021). (C) Enlarged geological map of the area in the red rectangle in Fig. 1B. The foliation and schistosity data are from Hisada et al. (1993). The location of the gabbro is from Seki and Kuriyagawa (1961). (D) Cross-section along the X–Y line in Fig. 1C (modified from Hisada et al., 1993). (E) Photograph in plan view of the Kanasaki area in the red rectangle in Fig. 1C, showing sample numbers, locations, and lithologies.

similar to those of the modern oceanic plateau basalt (Sano et al., 2012; Heydolph et al., 2014; Sager et al., 2016; Xia and Li, 2019). Distinguishing igneous rocks formed in oceanic plateaus from those formed in other tectonic settings often requires a combination of geological, petrological, and geochemical observations (Kerr et al., 2000; Pearce, 2008; Xia and Li, 2019). Such integrated observations have revealed that the Mikabu unit originated from an oceanic plateau derived from a depleted mantle source (Isozaki et al., 1990; Sakakibara et al., 1993; Kimura et al., 1994; Ozawa et al., 1997; Ichiyama et al., 2014; Sawada et al., 2019; Tominaga and Hara, 2021). These observations include: (i) the presence of picrites (Ichiyama et al., 2014), as high-Mg rocks (picrites and komatiites) are common in such settings but largely absent from mid-ocean ridge crust (Kerr, 2014); (ii) an estimated mantle potential temperature of 1650°C for the Mikabu picrites, consistent with temperatures inferred for picrites and komatiites in both oceanic and continental LIPs (Ichiyama et al., 2014); and (iii) the intercalation of pelagic sediments with mafic volcanic rocks within the Mikabu Unit (Sakakibara et al., 1993; Sawada et al., 2019). The presence of metachert xenoliths in diabase dikes further suggests that mafic magmas intruded into deep-sea cherts on the ancient ocean floor (Sakakibara et al., 1993; Sawada et al., 2019).

Zircon geochronology of a mafic rock from the Mikabu unit yielded a Late Jurassic age (154.6 ± 1.6 and 157.0 ± 0.9 Ma from Sawada et al. (2019) and Tominaga and Hara (2021), respectively), but slightly younger ages have also been reported (153 ± 3.6 – 146 ± 5.4 Ma; Ichiyama et al., 2018) , suggesting the emplacement of this oceanic plateau occurred at 157–146 Ma. The oceanic plateau was accreted at 125–110 Ma (Sawada et al., 2019; Tominaga and Hara, 2021), and then subsequently affected by greenschist-facies metamorphism. A chert xenolith in a doleritic dyke contains Middle Jurassic radiolarians (Tricolocapsa sp. and specimens tentatively identified as Williriedellum sp. and Protunuma sp.), indicating that the pre-existing Middle Jurassic (174–164Ma) deep-sea chert had been intruded by a younger mafic dyke (Sakakibara et al., 1993). Most researches suggest the Mikabu Plateau and Shatsky Rise (i.e., an oceanic plateau in the modern Pacific Ocean) might have been a single plateau that formed near the Kula–Pacific–Farallon triple junction during the Late Jurassic (Kimura et al., 1994; Tatsumi et al., 1998; Ichiyama et al., 2014; Sawada et al., 2019), although this is debated (Tominaga and Hara, 2021). The size of the Mikabu Plateau is unknown.

The ultramafic cumulates in the Mikabu unit include dunite, wehrlite, troctolite, and clinopyroxenite, which likely crystallized from a tholeiitic magma (Ishiwatari et al., 2016). Peridotitic restites have not been identified (Agata, 1994; Uesugi and Arai, 1999; Ichiyama et al., 2014; Ishiwatari et al., 2016). The K–Ar dating of hornblende from ultramafic cumulates in the Mikabu unit yielded ages of mostly 153–142 Ma (Ozawa et al., 1997), similar to the igneous age of the oceanic plateau.

The tectonic boundary between the Mikabu unit and proper Sanbagawa unit is composed mainly of pelitic schist of the proper Sanbagawa unit, with tectonic blocks of mafic volcanics and ultramafic rocks (including serpentinite) of the Mikabu unit (Tokuda, 1986; Makimoto and Takeuchi, 1992). The pelitic schists represent underplated sediments that were accreted following the progressive peeling-off of the Mikabu plateau (Tokuda, 1986; Makimoto and Takeuchi, 1992). This area has been referred as the ”Mikabu lower part” (Makimoto and Takeuchi, 1992) and was showed as ”Sanbagawa metamorphic rocks with tectonic blocks of the Mikabu unit” in Fig. 1B. The boundaries between the metapelite and serpentinite blocks are tectonic rather than sedimentary (Tokuda, 1986; Makimoto and Takeuchi, 1992).

The Kanasaki serpentinites are in the lower part of the Mikabu unit in the Kanto Mountains and occur as tectonic blocks in the Sanbagawa metapelites (Fig. 1B–D; Makimoto and Takeuchi, 1992). The surrounding metasediments in the study area have been assigned to the chlorite zone (Hashimoto et al., 1992). Similar temperatures (313 ± 13°C), based on Raman spectroscopy of carbonaceous matter, have been reported from a metasediment in the same metamorphic grade in the Kanto Mountains (Hara et al., 2021; Fig. 1B). The Kanasaki serpentinites are exposed across the Arakawa River (Fig. 1C–E). On the north side of the river, a large block of ultramafic rocks (20 m thick and 50 m long) is surrounded by greenschist-facies metasediments (Fig. 1C–E; Seki and Kuriyagawa, 1961; Hisada et al., 1993). Observation of the entire block is challenging due to the forest cover (Fig. 1E). No direct contact between the metasediments and ultramafic rocks has been observed, probably because it is obscured by thick leaf litter. However, the south bank of the river contains sporadic ultramafic blocks along with alluvium, with sizes of <5 × 5 m (Fig. 1E). A small occurrence of gabbro has been reported (Fig. 1C), which is strongly altered and composed by actinolite (14–24 vol.%), pumpellyite (32–35 vol.%), chlorite (22–38 vol.%), sodic plagioclase (10–16 vol.%), and titanite (3–4 vol.%) (Seki and Kuriyagawa, 1961). Currently, the gabbro outcrop is not observable, but gabbro boulders (<2 × 2 m) are observable.

III. METHODS

Mineral compositions were analyzed with an electron probe microanalyzer (EPMA; JEOL JXA-8500F) at JAMSTEC, Yokosuka, Japan, using an accelerating voltage of 15 kV and a beam diameter of 1–5 µm. The beam current was 1–10 nA for quantitative analysis, and 50 nA for element maps. Quartz (Si), rutile (Ti), corundum (Al), hematite (Fe), rhodonite (Mn), periclase (Mg), wollastonite (Ca), albite (Na), sanidine (K), and Cr_2O_3 standards were used for calibration. ZAF corrections were applied to convert raw data to wt.%. The stoichiometry and nomenclature of amphibole followed (Leake et al., 1997). Spinel composition was estimated by normalizing with three cations and four oxygens.

Raman analyses of carbonate and serpentine minerals were performed using a JASCO NRS-4100 laser Raman spectrometer at Kokushikan University. The wavelength of the laser source was 532 nm, and the laser power was set at 1–6 mW at the sample surface. Gratings with 900 or 1800 grooves mm^{-1} were used to disperse the wave. The objective lens was ×100, making the spatial resolution about 1 μm. The wave number was calibrated after measurement, using a polystyrene standard.

Carbonate C–O–Sr isotope analyses were conducted using a microdrilled carbonate powder (Table 1). Stable isotopes of carbonates were analyzed at Washington State University (WSU) and Niigata University (NU). For 13C and 18O analysis of carbonates at WSU, Gaseous samples for isotopic analysis were sampled with a two holed needle on a robotic autosampler (GC-PAL, CTC Analytics, Switzerland) and ThermoFinnigan GasBench II (Bremen) interface. Multiple gas species were separated at 40°C with a 25 m × 0.32 mm (inner diameter) GC column (Varian, poraplot Q) and analyzed with a continuous flow isotope ratio mass spectrometer (Delta PlusXP, Thermofinnigan, Bremen). Final delta values were based on the average of 5 sample peaks each time a vial was sampled. Isotopic reference materials were interspersed with samples for calibration. Solid sample and reference materials were converted to pure carbon dioxide from digestion with 100% phosphoric acid in helium flushed vials. Samples were maintained at 25°C for the digestion (24–48 hour) and during the analysis. Carbon isotopic results were reported in per mill relative to VPDB (Vienna Peedee belemnite). Oxygen isotopic results were reported in per mill relative to VPDB and converted to those relative to VSMOW (Vienna Standard Mean Ocean Water). The $\pm 1\sigma$ values of $\delta^{13}C_{VPDB}$ and $\delta^{18}O_{VSMOW}$ for NBS-18 were ±0.12‰ and ±0.2‰, respectively (Table 2).

The stable isotope analysis of carbonates at NU were conducted as follows. Carbonate powder samples were placed in small stainless-steel thimbles and dropped into a reaction vessel containing pyrophosphoric acid at 60°C in a vacuum to liberate CO_2 gas. The CO_2 was cleaned cryogenically to remove impurities such as H_2O with pentane slush and collected using a liquid nitrogen cold trap. Stable-isotope measurements were carried out with a Thermo Fisher MAT-253 mass spectrometer. The precisions of $\delta^{13}C_{VPDB}$ and $\delta^{18}O_{VSMOW}$ values for the laboratory standard CO_2 gas were ±0.03‰ and ±0.05‰, and for NBS-20 were ±0.05‰ and ±0.1‰, respectively (Table 2).

Strontium isotopes were measured using the same aliquots than for stable isotopes and bulk trace element analyses. Carbonate were firstly decomposed in a mixed solution of distilled water and CH_3COOH in a Teflon® vessel. Only carbonate minerals dissolve in acetic acid, which minimizes the effect of any minor silicate minerals, especially detrital components, on the strontium isotopic composition. After dissolution, the vials were centrifuged, and the supernatant was separated. Distilled water was added once again to the residue, and the supernatant was collected. The collected supernatant liquid was evaporated to dryness and nitric acid was added to the residue. Ca–Rb–Sr and REEs were separated in a first column separation (BioRad, AG50W-X8 cation exchange resin).

Purification of strontium was undertaken with a second column separation (Eichrom Sr-Spec resin). Strontium isotope analyses were carried out following the procedures of Miyazaki and Shuto (1998) by thermal ionization mass spectrometry with a Finnigan MAT 262 mass spectrometer at NU. A tantalum (sample) and rhenium (ionization) filament combination were used for the analysis. Strontium isotope compositions were normalized to $^{87}Sr/^{86}Sr = 0.1194$. Repeated measurements of the strontium isotopic composition of the NIST 987 standard ($^{87}Sr/^{86}Sr = 0.710251 \pm 0.000003$; 2σ; n = 20) agreed well with the known values for this standard (0.710248; McArthur et al., 2020) (Table 2). Initial $^{87}Sr/^{86}Sr$ ratios were obtained by correcting the measured compositions for radiogenic ^{87}Sr produced from ^{87}Rb decay (Faure and Mensing, 2004), using Rb and Sr concentration determined by ICP-MS analysis of bulk carbonate. Because of the very low carbonate Rb/Sr ratio (Rb/Sr $<10^{-4}$; Table 2), the differences between the initial and present-day $^{87}Sr/^{86}Sr$ ratios are smaller than the analytical error (Table 2).

Trace element compositions of carbonates were obtained by bulk and in-situ analysis. For bulk analysis, carbonate sample powders (20–50 mg) were placed into vials containing 0.5 mL of distilled water and 0.2 mL of CH_3COOH. After dissolution and drying, a mixed acid solution (nitric, hydrochloric, and hydrofluoric acids) was used to dissolve the powders, which were then dried three times. All analyses were carried out using an inductively coupled plasma mass spectrometer (ICP-MS) instrument at NU, using the procedures of Neo et al. (2009). Anomaly of Ce (Ce/Ce*) and Eu (Eu/Eu*) was calculated by $Ce_{SN}/(Pr_{SN}^2/Nd_{SN})$ and $Eu_{SN}/(Sm_{SN}^2Tb_{SN})^{1/3}$, respectively (Lawrence et al., 2006), where the subscript SN indicate the shale-normalized value. The Pr_{SN}/Yb_{SN} ratio were used for evaluating enrichments/depletion of light REE (LREE) relative to heavy REE (HREE). Trace element compositions are given in Table 2, and the entire dataset is provided in Table S1 in the Supplemental Material (`https://doi.org/10.1130/GSAB.S.29832038`).

In-situ trace element composition of carbonate was analyzed by laser ablation inductively coupled plasma mass spectrometer (LA-ICP-MS) at JAMSTEC; the analysis was performed using a 266 nm femtosecond LA system (OK-Fs2000K, OK Laboratory, Japan) coupled to a single-collector sector field–type ICPMS (SF-ICP-MS, Element XR, Thermo Fisher Scientific, Bremen, Germany). A thick (∼150 μm) polished section was used. Measurements were carried out in low resolution and electrostatic scanning (E-scan) modes. Laser ablation of samples was performed with single spot size of 70 μm in diameter, using a repetition rate of 100 Hz and a fluence of ~ 12 J cm^{-2} (Kimura and Chang, 2012). Analytes analyzed include Li, B, As, Rb, Sr, Y, Zr, Nb, Sb, Cs, Ba, Re, REEs, Hf, Ta, W, Th, and U. In addition, ^{43}Ca and ^{29}Si were measured as internal standards. The concentration of Ca and Si in a given mineral was estimated based on stoichiometry. As a calibration standard, NIST SRM610 standard glass was used. To check analytical accuracy, this study analyzed BCR-2G glass provided by the United States Geological Survey (Jochum et al., 2005) and obtained results in good agreement with reference values except for As (Table S2). Accuracies were <5% for most elements except Li (9.7%), B (11.8%), Lu (5.5%), W (6.6%), and U (6.7%) (Table S2). The analytical data of the in-situ trace elements composition are provided in Table S3.

The LA-ICP-MS analysis showed that calcite in the studied samples has a wide range of Sr/Ca molar ratio ($[\frac{Sr}{Ca}]_{Calcite}$).

Fluid Sr/Ca molar ratio ($[\frac{Sr}{Ca}]_{Fluid}$) can be determined from $[\frac{Sr}{Ca}]_{Calcite}$ by:

$$\left[\frac{Sr}{Ca}\right]_{Fluid} = \frac{\left[\frac{Sr}{Ca}\right]_{Calcite}}{K_{Sr}^{eq}}, \tag{1}$$

where K_{Sr}^{eq} is the equilibrium partition coefficient between calcite and fluid. The temperature (T; in K) dependent partition coefficients were given by;

$$K_{Sr}^{eq} = 0.025 \exp\left(\frac{\Delta G_{r,0}}{R}\left(\frac{1}{298.15} - \frac{1}{T}\right)\right), \tag{2}$$

which is applicable for the temperature range 0–200°C (Zhang and DePaolo, 2020). $\Delta G_{r,0}$ (= 5.0 kJ mol^{-1}) is the free energy change associated with the exchange reaction and temperature (T) is in Kelvin. R (J K^{-1} mol^{-1}) is the gas constant.

IV. RESULT

A. Field and geometrical analyses

The Kanasaki serpentinites exhibit variable degrees of carbonation, with carbonate modal abundances ranging from <5 vol.% to as high as 60 vol.%. Based on the dominant carbonate minerals and their occurrence, four types of carbonates were identified in the carbonate-bearing serpentinite (ophicarbonate): calcite (Cal) cement in brecciated serpentinite (type I carbonate; Fig. 2A), dolomite (Dol) + Cal cement in brecciated serpentinite (type II carbonate; Fig. 2B), and discrete veins of calcite (type III carbonate; <1–50 mm in width; Fig. 2C, D) and dolomite + calcite (type IV carbonate; ∼10 mm in width; Fig. 2B). Type I is the dominant type of carbonate in the study area, whereas ophicarbonate with the other carbonate types (II, III, and IV) is less common and concentrated in the eastern domain (Fig. 1E). Field observations indicate the type IV carbonate (Dol + Cal veins) cuts the ophicarbonate with type II carbonate (Fig. 2B), and the type III carbonate (Cal veins) cuts the serpentinite (Fig. 2C) and ophicarbonate with type I carbonate (Fig. 2D). Other structural relationships are not clear from the field observations, because: (1) outcrops are sparse in the Kanasaki area (Fig. 1E); and (2) the outcrops on the northern side of the river occur in forest (Fig. 1E).

B. Petrography

1. *Serpentinite*

Two types of serpentinites were observed: massive serpentinite and bastite serpentinite (Table 1). The massive serpentinite mainly consists of serpentine with minor amounts of chlorite, spinel, ilmenite, apatite, and Fe sulfide (Fig. 3A). No relicts of primary olivine were observed. Lacking bastite in the massive serpentinite imply protolith of the massive serpentinite is dunite. The serpentinite matrix has a typical mesh texture, consisting of dark gray-colored mesh cores and yellowish rims under cross-polarized light (Fig. 3A, B). Raman spectroscopy suggests that the mesh core is predominantly made of lizardite, but chrysotile mesh cores have also been observed. The mesh rim serpentinite is antigorite. Ilmenite occurs as porous elongate grains in the serpentine matrix with sizes of ∼100 µm (Fig. 3C). The bastite serpentinite tends to occur in the eastern part of the study area (Fig. 1E; Table 1). No relicts of primary olivine or pyroxene were observed. Mineral assemblages in the bastite serpentinite are similar to those in the massive serpentinite. The bastite serpentinite contains bastite, along with serpentine, and lacks Ca-bearing minerals (e.g., tremolite and diopside). Some of bastite and serpentine matrix is cut by later serpentine (antigorite or lizardite) veins (Fig. 3F). In the massive serpentinite and bastite serpentinite, no primary spinel was observed. Apatite occurs in the mesh core in the serpentine matrix or as intergrown crystals (mostly ∼100 µm but some up to 500 µm in size) with the antigorite vein.

2. *Ophicarbonate with type I carbonate*

Ophicarbonate with type I carbonate occurs as brecciated clasts of serpentine with a calcite cement, and is the dominant lithology in the study area (Figs 1E and 2A; Table 1). The serpentine clasts are fully serpentinized peridotites (dunites) and lack relict olivine. The serpentine breccia has a jigsaw-puzzle-like texture (Figs 4A, B and S1A) and exhibits similar mesh textures as the carbonate-poor serpentinites (Fig. 4B). In addition, in plane- and cross-polarized light, some serpentinite clasts contain cloudy to black-colored serpentine areas surrounded by light green-colored serpentine (Fig. 4C). Backscattered electron imaging suggests that the former serpentine contains abundant pores with sizes of <1–10 µm (Fig. 4D), which may have resulted from leaching/weathering of carbonate minerals under subsurface conditions. Calcite cementing the serpentine clasts occurs as coarse grains with twinning that have aggregates of fine grains along their rims (Fig. 4E). Primary spinel is mostly altered to magnetite, but is preserved in two ophicarbonate samples (KN22093004 and KN23011003). Primary spinel crystals have a brownish core under plane-polarized light, and occur as inclusions in calcite (Fig. 4F) and in the serpentine matrix (Fig. 4G) in samples KN22093004 and KN23011003, respectively. The spinel composition is similar regardless of occurrence (Fig. 4F, G), with a wide range of compositions and Cr/(Cr + Al) = 0.39–0.70 and Mg/(Mg + Fe^{2+}) = 0.35–0.64 (Fig. 5A–B; Table S4). Spinel $\mathrm{TiO_2}$ contents are <0.22 wt.%.

Brown (Fig. 6A) and colorless amphibole (Fig. 6B) are observed in the serpentine matrix in some samples (KN23011002 and KN23011004). Brown amphibole (Fig. 6A) occurs as subhedral crystals (100–200 µm) in the serpentine matrix and contains inclusions of ilmenite (Fig. 6C). The brown amphibole showed ambiguous growth zoning, but Si-poor and Ti-rich part and Si-rich and Ti-poor parts were observed (Fig. 6C). The brown amphibole is rich in $\mathrm{Na_2O}$ (1.66–3.15 wt.%; Fig. 6D) and $\mathrm{TiO_2}$ (1.66–2.40 wt.%; Fig.

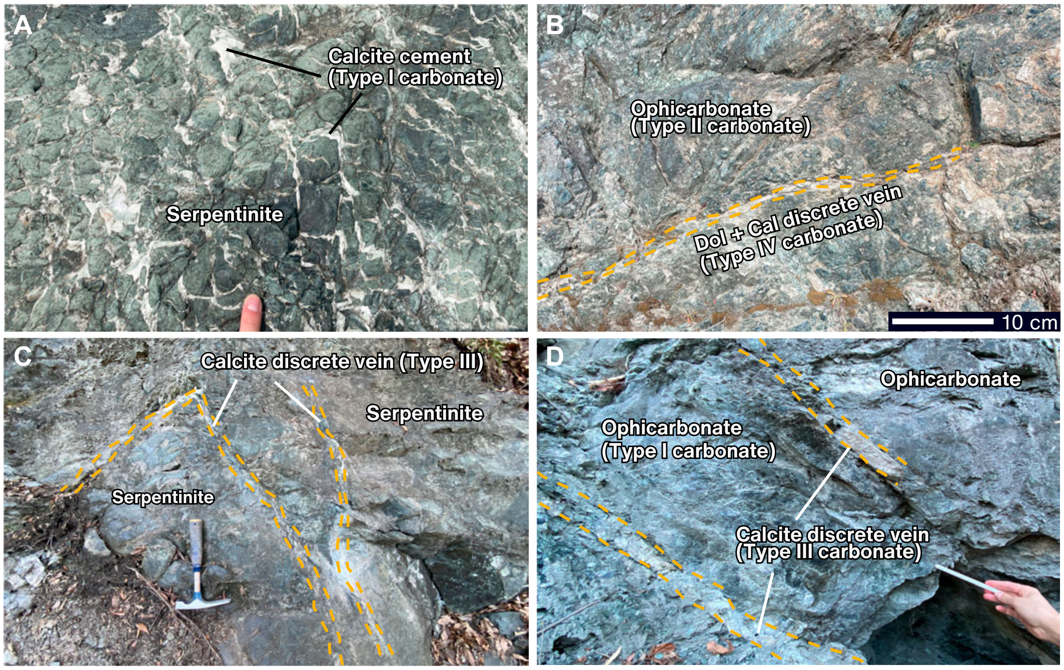

FIG. 2. (A) Outcrop of ophicarbonate consisting of calcite cement and brecciated serpentinite (type I carbonate; 36°04’47”N, 139°05’51”E). (B) Outcrop of ophicarbonate consisting of dolomite + calcite cement and brecciated serpentinite (type II carbonate), which is crosscut by later discrete dolomite + calcite veins (type IV carbonate; 36°04’49”N, 139°05’52”E). (C) Serpentinite with a discrete calcite vein (type III carbonate; 36°04’52”N, 139°05’51”E). (D) Ophicarbonate matrix (brecciated serpentinite and calcite cement [type I carbonate]) crosscut by a discrete calcite vein (type III carbonate) (36°04’52”N, 139°05’52”E).

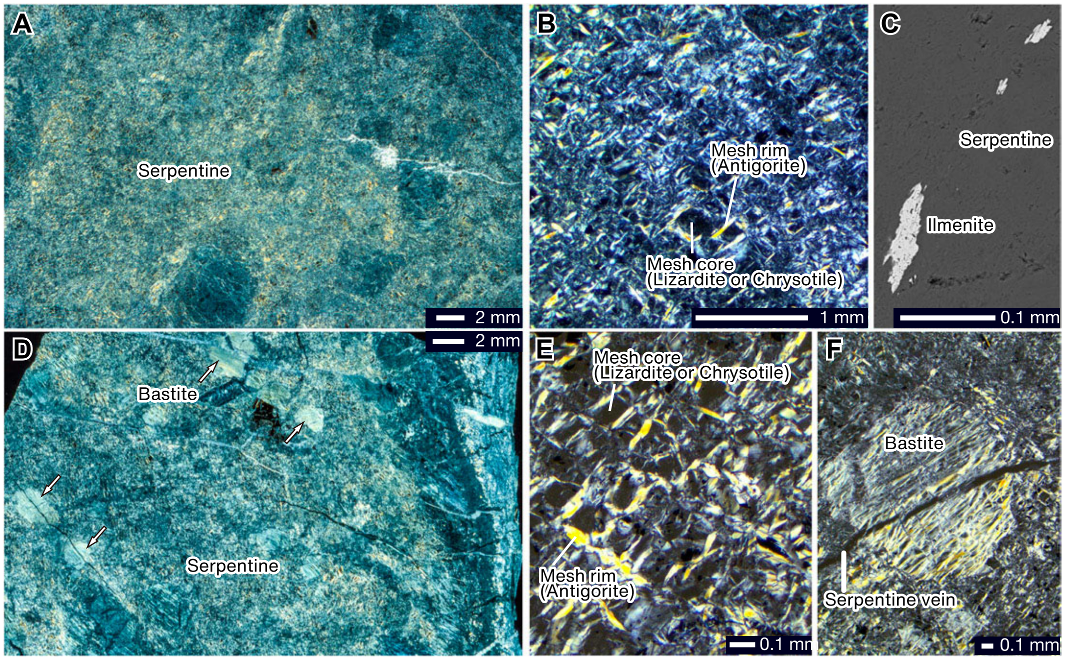

FIG. 3. (A–C) Photomicrographs of serpentinite (massive serpentinite). (A) Whole thin-section image of serpentinite under cross-polarized light (sample KN22093008). (B) Mesh texture of the serpentine matrix (sample KN22093008). (C) Occurrence of ilmenite in the serpentine matrix (sample KN22093013). (D–F) Photomicrograph of a serpentinite (bastite serpentinite; sample KN220423). (D) Whole thin-section image of a bastite serpentinite under cross-polarized light. The white arrows indicate bastite. (E) Mesh texture of the serpentine matrix. (F) Bastite crosscut by a serpentine (lizardite) vein.

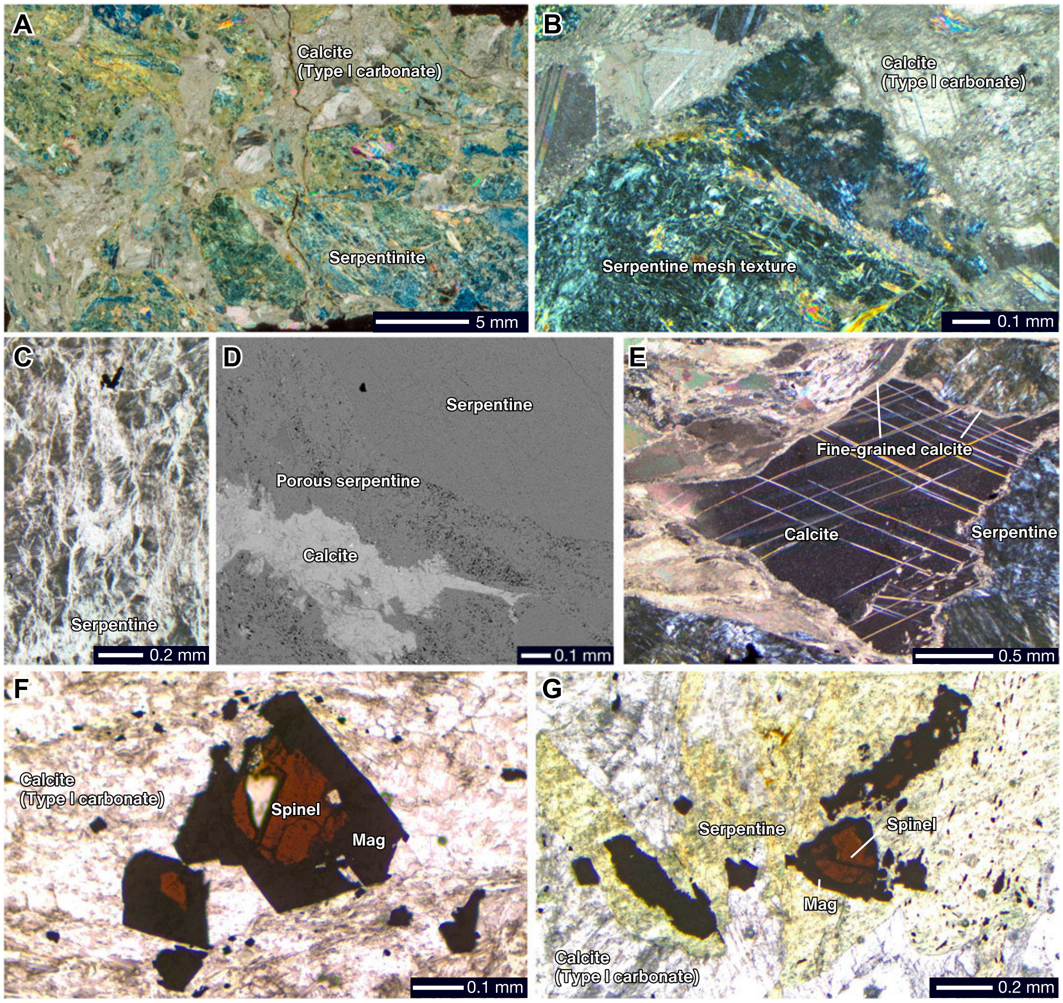

FIG. 4. (A) Whole thin-section image of typical ophicarbonate (type I) under cross-polarized light (sample KN23011004). (B) Occurrence of serpentinite clasts in the ophicalcite (sample KN23011004). Both a mesh texture and massive serpentine were observed in the clasts, similar to the carbonate-poor serpentinite (Fig. 3B, E). (C–D) Occurrence of a porous domain in the serpentine clasts in the ophicalcite under plane-polarized light (C) and a backscattered electron (BSE) image of this domain (D; sample KN22072501). (E) Calcite crystal in ophicalcite, showing twinning (sample KN22072501). (F–G) Spinel in the ophicarbonate (F; sample KN22093004) and serpentine matrix (G; sample KN23011003), which contains relict primary chromite in its core and an overgrown magnetite rim.

6E), and can be classified as pargasite, edenite, tschermakite, magnesio-hornblende, and magnesio-hastingsite (Table S5). The colorless amphibole occurs as isolated grains (Fig. 6B). The isolated colorless amphibole shows compositional zoning, with cores mostly of magnesio-hornblende and rims of actinolite (Fig. 6F; Table S5). The Na_2O and TiO_2 and of the colorless amphibole are 0.26–2.00 wt.% (Fig. 6D) and 0.00–0.41 wt.% (Fig. 6E), respectively.

3. *Ophicarbonate with type II carbonate*

Ophicarbonate with type II carbonate occurs as brecciated clasts of serpentinite with a dolomite + calcite cement (Fig. 7A, B), and consists of serpentine, dolomite, and calcite. Serpentinite breccias have rounded grains and a jigsaw-puzzle-like texture (Fig. 7A). Bastite and relict minerals (olivine) were not observed in the serpentine matrix. The dolomite in the cement shows coarse blocky grains with twinning and a heterogeneously distributed brecciated part (hereafter microbreccia) (Fig. 7B). Calcite occurs along the cleavage in the blocky dolomite crystal and as cement of the microbreccia (Fig 7C). The backscattered electron image of the microbreccia domain shows that certain fine dolomite is dark (Fig. 7D). Bright dolomite occurs in coarse blocky grains and the microbreccia. The dark dolomites are slightly enriched in Mg (Mg/(Mg+Fe+Ca) = 0.49) compared to the bright dolomite (Mg/(Mg+Fe+Ca) = 0.47) (Table S6). Primary spinel occurs in the serpentine matrix in some samples (KN22093009 and KN22093010), with Cr/(Cr + Al) = 0.61–0.64, Mg/(Mg + Fe^{2+}) = 0.55–0.59 (Fig. 5A–B), and TiO_2 <0.10 wt.% (Table S4).

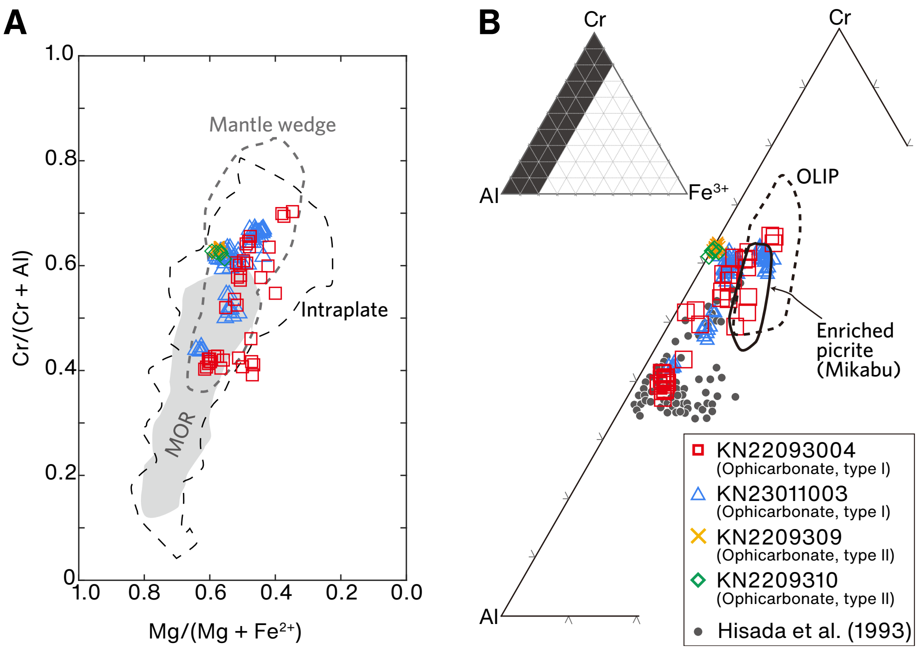

FIG. 5. Compositions of spinel from the Kanasaki serpentinites. (A) Plot of atomic Mg/(Mg + Fe^{2+}) versus Cr/(Cr + Al). The compositional fields for mid-ocean ridge (MOR) and mantle wedge peridotites are from (Tamura and Arai, 2006), and for intraplate dunites are from Arai (2011). (B) Cr–Al–Fe^{3+} ternary plot for spinel. The compositional fields for oceanic large igneous provinces (OLIP) and enriched picrites are from Ichiyama et al. (2014) and references therein.

4. *Ophicarbonate with type III carbonate*

Type III carbonate occurs in discrete calcite veins that are planar (<1–50 mm in width) and cut the serpentinite (Fig. 2C) or ophicarbonate (type I) matrix (Fig. 2D). The discrete calcite veins are sparsely distributed and concentrated in the eastern part of the study area (Fig. 1E). The dolomite crystals in the discrete veins are blocky and twinned (∼5 mm in size) (Fig. 7E). No other carbonate minerals were observed. The discrete calcite veins contain serpentinite fragments (Fig. 7E, F), and some showed continuous microtexture with the host-rock serpentinite (Fig. 7F). Primary spinel was not observed.

5. *Ophicarbonate with type IV carbonate*

The type IV carbonate occurs as discrete dolomite + calcite veins, which were observed in one sample (KN22093011; Fig. 7A; Table 1). The type IV carbonate crosscuts the matrix of ophicarbonate with type II carbonate (Fig. 7A). Similar to type II carbonate, type IV carbonate shows coarse grained dolomite and microbreccia domain. Dolomite crystals in the discrete veins occurs as blocky crystal and twinned with grain size of 0.5–1.0 mm (Fig. 7G). Calcite occurs along cleavage in the dolomite crystals (Fig. 7G) and as cement of the microbreccia (Fig. 7H). The fragmented dolomite crystals in the microbreccia are partly Mg-rich (Fig. 7I).

C. Carbonate geochemistry

The C–O–Sr isotope and bulk trace element data for the carbonates are summarized in Table 2. The $\delta^{18}O_{VSMOW}$ and $\delta^{13}C_{VPDB}$ values of the type I carbonates range from +13.31‰ to +15.69‰ and –1.81‰ to +2.02‰, respectively (Fig. 8A). The type II carbonate has $\delta^{18}O_{VSMOW}$ values of +14.71‰ to +19.22‰ and $\delta^{13}C_{VPDB}$ values of –7.53‰ to –6.88‰. The values for the type III carbonate are +13.31‰ to +16.29‰ and –8.07‰ to –5.95‰, and those for the type IV carbonate are +15.71‰ to +16.42‰ and –7.18‰ to –7.35‰. The type I carbonate has $\delta^{13}C_{VPDB}$ values close to 0‰, whereas the other carbonate types (II, III, and IV) have lower $\delta^{13}C_{VPDB}$ values (Fig. 8A). The carbonate $\delta^{13}C_{VPDB}$ values are typically elevated on the western side of the study area and relatively low on its eastern side (Fig. S2). Variations of $\delta^{18}O_{VSMOW}$ and $\delta^{13}C_{VPDB}$ in a single sample were investigated for selected samples (Table 1), which revealed that the $\delta^{18}O_{VSMOW}$ values had large variations (ranging from 0.6‰ to 6‰) in a single sample, whereas $\delta^{13}C_{VPDB}$ values had less variation (<0.2‰; Fig. S1A–C).

Present-day $^{87}Sr/^{86}Sr$ ratios vary from 0.7063 to 0.7083 and are generally higher for lower-$\delta^{13}C_{VPDB}$ carbonate (Fig. 8B). The most radiogenic $^{87}Sr/^{86}Sr$ value (∼0.7083) was observed for the type II, III, and IV carbonates, whereas the most unradiogenic $^{87}Sr/^{86}Sr$ value (∼0.7063) was obtained for some type I carbonates.

The type I carbonate has variable REE patterns (Fig. 9A). REE patterns with negative Ce anomalies (Ce/Ce* = 0.23–0.61), small positive Eu anomalies (Eu/Eu* =

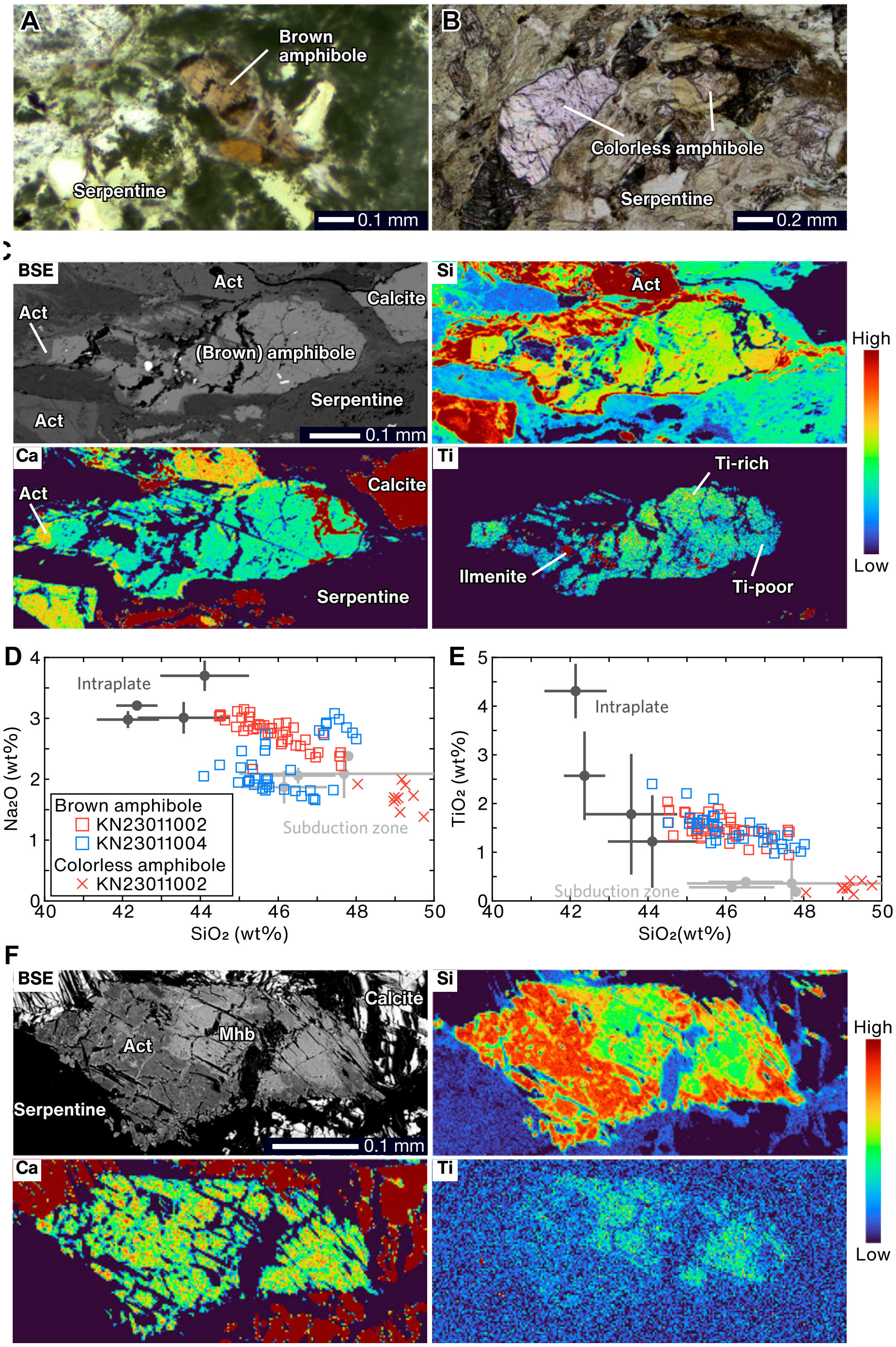

FIG. 6. (A) Brown amphibole in the serpentine matrix of ophicarbonate (sample KN23011002) under plane-polarized light. (B) Colorless amphibole in the serpentine matrix of ophicarbonate (sample KN23011004) under plane-polarized light. (C) Backscattered electron (BSE) image and elemental maps (Si, Ca, Ti) of brown amphibole in the serpentine matrix of ophicarbonate (sample KN23011004). (D–E) Compositions of amphibole in the Kanasaki serpentinites. Plots of Na_2O versus SiO_2 (D) and TiO_2 versus SiO_2 (E). Dark and light gray circles are amphibole compositions for intraplate and subduction zone settings, respectively (Coltorti et al., 2007). Error bars are $\pm 1\sigma$. (F) BSE image and elemental maps (Si, Ca, Ti) of colorless amphibole in the serpentine matrix of ophicarbonate (sample KN23011004). Act, actinolite. Mhb, magnesio-hornblende.

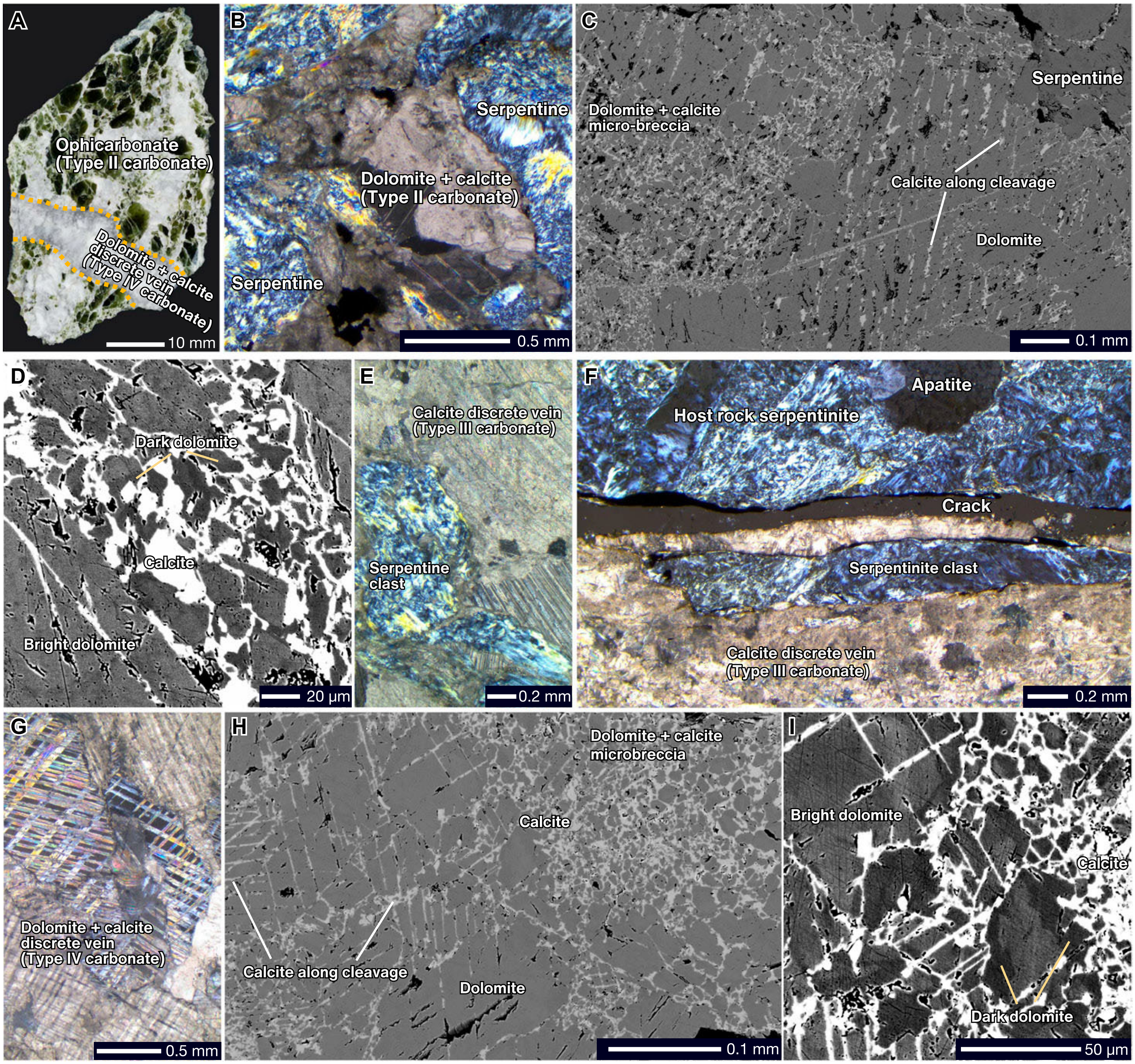

FIG. 7. (A) Polished section of ophicarbonate (type II) with a discrete dolomite + calcite vein (type IV; sample KN22093011), showing ophicarbonate matrix crosscut by the vein. (B) Representative photomicrograph of ophicarbonate matrix under cross-polarized light (sample KN22093011). (C) Backscattered electron (BSE) image of ophicarbonate (type II). Calcite (light gray) occurs along cleavage in a dolomite crystal (dark grey). Partly, dolomite and calcite form micro-sized breccia. (D) BSE image of the dolomite + calcite micro breccia in the ophicarbonate (type II; sample KN22093011). Dark (Mg-rich) dolomite crystals are partly observed. (E–F) Representative photograph of a discrete calcite vein (type III). (E) Serpentinite clasts in the discrete calcite vein under cross-polarized light (sample KN22072503). Calcite in the discrete vein exhibits twinning. (F) Photomicrograph of the boundary between host rock serpentine and a discrete calcite vein under cross-polarized light (sample KN22093014). The serpentinite clast is texturally continuous with the host rock serpentinite. (G–I) Representative photograph of a discrete dolomite + calcite vein (type IV). (G) Photomicrograph of a discrete dolomite + calcite vein under cross-polarized light (sample KN22093011) (H) BSE image of a discrete dolomite + calcite vein (tsample KN22093011). Calcite (light gray) occurs along cleavage in a dolomite crystal (dark grey). Partly, dolomite + calcite form micro breccia. (I) BSE image of dolomite + calcite micro breccia in the ophicarbonate (sample KN22093011). Dark (Mg-rich) dolomite crystals are partly observed.

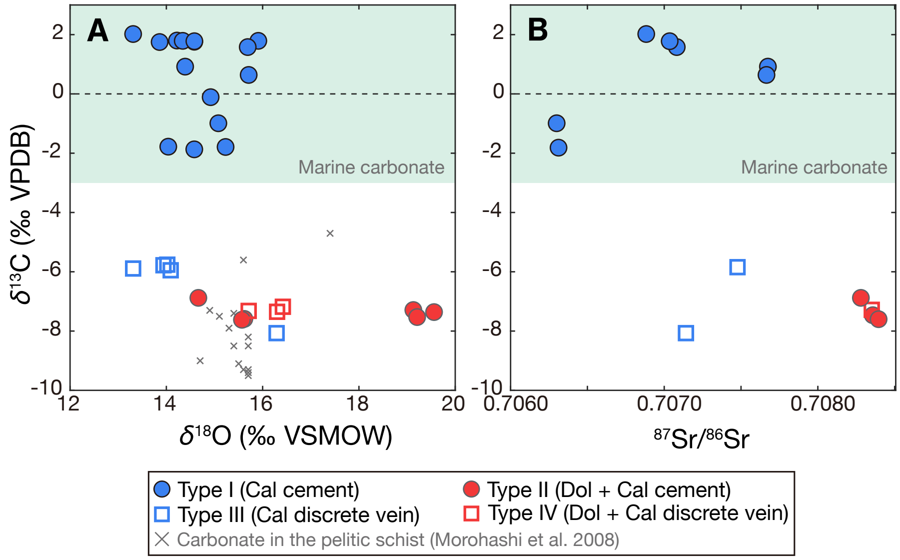

FIG. 8. (A) $\delta^{18}O_{VSMOW}$ (VSMOW = Vienna standard mean ocean water) and (B) present-day $^{87}Sr/^{86}Sr$ versus $\delta^{13}C_{VPDB}$ (VPDB = Vienna Peedee belemnite) for the carbonates. The light gray region is the $\delta^{13}C_{VPDB}$ range of typical marine carbonates (Ripperdan, 2001). The gray crosses indicate the C-O isotopic compositions of carbonates hosted in metasediments (Morohashi et al., 2008) taken from the locations indicated in Fig. 1B.

1.13–1.36), and light REE depletion relative to heavy REEs (Pr_{SN}/Yb_{SN} = 0.13–0.69) characterize some type I carbonate (samples KN22072501 and KN22093004; Fig. 9A; Table 2). In contrast, one sample of type I carbonate (KN22093014) has a distinct REE pattern, characterized by the lack of Ce anomaly (Ce/Ce* = 0.96), a pronounced positive Eu anomaly (Eu/Eu* = 13.09), and light REE enrichment relative to heavy REEs (PrSN/YbSN = 1.89; Fig. 9A; Table 2). Intermediate REE patterns, characterized by both negative Ce (Ce/Ce* = 0.67–0.80) and positive Eu (Eu/Eu* = 2.45–3.66) anomalies, characterize the other carbonate samples (KN22093012, KN23011002, KN23011006, and KN23011007; Fig. 9A; Table 2). Broad correlations between Ce or Eu anomalies and $\delta^{13}C_{VPDB}$ values were observed for the type I carbonate. With decreasing $\delta^{13}C_{VPDB}$ values of type I carbonate from +2.02‰ (sample KN22093004) to –1.81‰ (sample KN22093014), the negative Ce anomaly becomes smaller (Ce/Ce* values of 0.23 to 0.96; Fig. 9C), and the Eu anomalies become larger (Eu/Eu* values of 1.13 to 13.09; Fig. 9D). The U concentrations of the type I carbonate are <0.070 mg kg^{-1} (Tables 2 and S1).

The REE patterns of type II, III, and IV carbonates are uniformly characterized by marked positive Eu anomalies (Eu/Eu* = 4.41–20.19; Fig. 9A, B; Table 2). The type II carbonate exhibits light REE depletion relative to heavy REEs (Pr_{SN}/Yb_{SN} = 0.12–0.13; Fig. 9A, D). For the type II, III, and IV carbonates, the Ce anomaly is not apparent (Ce/Ce* = 0.91–0.98; Fig. 9C). The U concentrations of type II, III, and IV carbonates are <0.001 mg kg^{-1} (Tables 1 and S1). In general, in situ trace element analysis of the type I–IV carbonates yielded broadly similar results than the bulk carbonate analysis (Fig. 9C, D).

V. DISCUSSION

A. Conditions of serpentinite carbonation

The occurrence of pargasitic amphiboles in the ultramafic rock has been reported in the Mikabu unit, and Inomata and Tazaki (1974) proposed that the pargasitic amphiboles were crystallized by reaction between alkali basaltic melt and olivine and clinopyroxene in the mantle rocks. The pargasitic brown amphibole observed in the present study could have a similar origin. Contrary, the colorless amphibole would be would be of metamorphic origin, recrystallizing after clinopyroxene. The porous ilmenite in the serpentine matrix (Fig. 3C) could be of metamorphic origin that most likely recrystallized from Ti hosted in spinel. Apatite would be also of metamorphic origin as it occurs in the mesh core of the serpentinites and in the serpentine vein.

The microtextural relationships (Fig. 7E, F) suggest that the ultramafic rocks underwent serpentinization followed by carbonation. The Mikabu unit has experienced a complex geological history from igneous activity during the formation of oceanic lithosphere to subsequent accretion and metamorphism. Therefore, the carbonate could have obtained its carbon isotopic signature from various sources, such as the mantle, seawater, hydrothermal fluids, and slab-derived devolatilization fluids generated during metamorphism. Our geochemical data indicate two potential origins for the carbonate minerals in the serpentinized ultramafic cumulates, based on carbonate $\delta^{13}C_{VPDB}$ values. The $\delta^{13}C_{VPDB}$ values of marine carbonates are typically ∼0‰ (Alt and Teagle, 2003; Bach et al., 2011) and have been 0‰ ± 3‰ for most of the last 3.5 Gyr (Ripperdan, 2001). The type I carbonate has $\delta^{13}C_{VPDB}$ values typical of marine carbonates, but the type

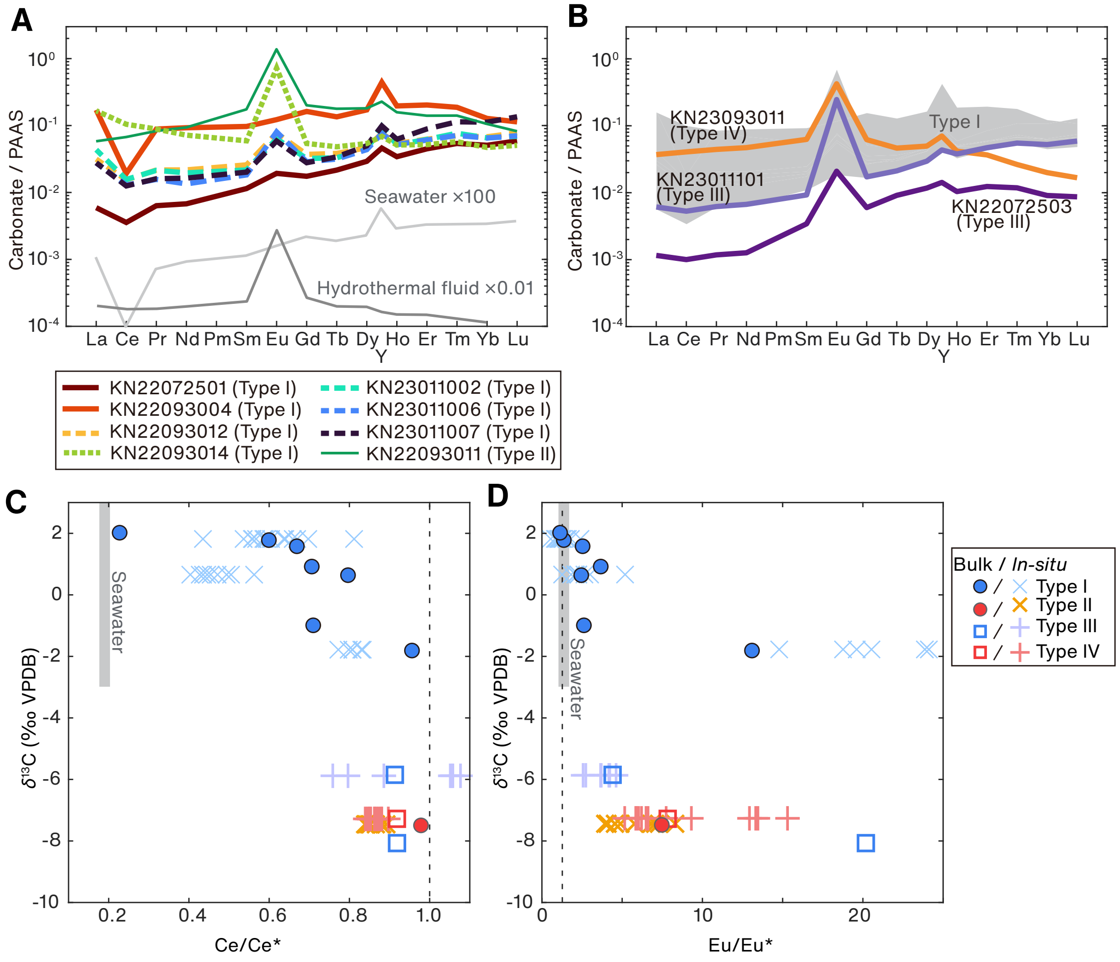

FIG. 9. (A) Rare earth element (REE) data for bulk type I and II carbonate normalized to Post-Archean Australian Shale (PAAS; Pourmand et al., 2012). The compositions of the seawater and an ultramatic-hosted hydrothermal vent fluid are from Schmidt et al. (2007). (B) PAAS-normalized bulk REE pattern of type III and IV carbonates. The gray region indicates the range of type I carbonate data shown in Fig. 9A. (C–D) Plot of carbonate $\delta^{13}C_{\mathrm{VPDB}}$ values versus Ce (Ce/Ce*) and Eu (Eu/Eu*) anomalies, respectively, from bulk and in situ analysis. In (C–D), the dotted black lines indicate the threshold value (1) for Ce/Ce* and Eu/Eu*, whereas the gray areas indicate the seawater values. For Ce/Ce* and Eu/Eu*, values of <0.9 and >1.1 are statistically significant negative and positive anomalies, respectively.

II–IV carbonates deviate from this marine range (Fig. 8A), suggesting there were different carbon sources for the type I and II–IV carbonates.

1. *Type I carbonate*

The $\delta^{13}C_{\mathrm{VPDB}}$ values of the type I carbonate (–1.81‰ to +2.02‰) are comparable to the range defined for marine carbonates (Fig. 8A), and dissolved inorganic carbon in seawater was likely the source of the carbon. In addition, the REE patterns of type I carbonate could be indicative of a contribution from seawater and hydrothermal fluids. The REE pattern of seawater is typically characterized by heavy REE enrichment, and negative Ce and positive Y anomalies (Fig. 9A; e.g., Smrzka et al., 2019). The negative Ce anomaly in seawater is caused by preferential adsorption onto particles and Ce(III) being partially oxidized to Ce(IV) and adsorbed to the surface of Mn (oxyhydr)oxides under oxidizing conditions (German and Elderfield, 1990). In contrast, the redox behavior of Eu is more strongly controlled by pH and temperature (Elderfield, 1988), and hydrothermal fluids that have undergone dissolution of Ca-bearing mineral (e.g., plagioclase) are characterized by positive Eu anomalies (Klinkhammer et al., 1994). The observed Eu anomalies in the type I carbonate (sample KN22093014; Fig. 9A) indicate a contribution from such hydrothermal fluids. The broad trend of increasing Eu/Eu* with decreasing $\delta^{13}C_{\mathrm{VPDB}}$ for the type I carbonate (Fig. 9D) implies that the hydrothermal fluids reacted with plagioclase-bearing lithologies were ^{13}C-depleted, presumably due to a contribution from magmatic volatiles ($\delta^{13}C_{\mathrm{VPDB}}$ = –11‰ to –3‰; McCollom, 2008).

The $\delta^{18}O_{\mathrm{VSMOW}}$ values of the type I carbonate (Fig. 8A, B) are lower than those of Phanerozoic marine carbonates formed at ambient seawater temperatures ($\delta^{18}O_{\mathrm{VSMOW}} \sim 30$‰; e.g., Veizer and Prokoph, 2015). Formation temperatures of type I carbonates can be estimated from carbonate-water fractionation factors of oxygen isotope, but an additional uncertainty is introduced by possible resetting of the isotopic composition (e.g., Fruh-Green et al., 1990; Coltat et al., 2019, 2021; Bernoulli and Weissert, 2021a, b) during the greenschist-facies metamorphism of the Kanasaki serpentinites via the oxygen diffusion and the fluid-mediated dissolution-reprecipitation mechanisms. Assuming a duration of 1–10 Myr at a peak metamorphic temperature of 400°C (plausible duration of the Mikabu unit metamorphism; Takasu and Dallmeyer, 1990) and using the oxygen diffusion coefficient of calcite (Labotka et al., 2000), a characteristic diffusion distance for oxygen of 4–12 μm is obtained. Hence, we estimate that diffusive exchange is too slow to change the isotopic composition of the carbonates. Moreover, if the fluid-mediated dissolution-reprecipitation of calcite occurred, REE pattern would be similar for all types of carbonates. However, this is not the case (Fig. 9A, B). Overall, we consider that re-equilibration of oxygen isotope compositions would not occur during subsequent greenschist metamorphism and therefore the oxygen isotope compositions of type I ophicarbonates would be indicative of oceanic alteration conditions. The $\delta^{18}O_{VSMOW}$ values of ambient seawater and seawater circulating in oceanic serpentinite are ∼0‰ and ∼2‰, respectively (Sakai et al., 1990; Früh-Green et al., 2003). Using $\delta^{18}O_{VSMOW}$ for water of 0‰ to +2‰, and the oxygen isotopic fractionation factor between calcite and water (Kim and O'Neil, 1997; Daëron et al., 2019), $\delta^{18}O_{VSMOW}$ values of the type I carbonate indicate formation temperatures of 120–160°C.

Metastable aragonites are common in modern oceanic serpentinites and typically formed at 0–15°C by interaction between seawater and ultramafic rock (Eickmann et al., 2009; Bach et al., 2011; Oyanagi et al., 2021; Ternieten et al., 2021). The estimated formation temperature for the type I carbonate (120–160°C) is higher than typical temperatures for the metastable aragonite precipitation on the present-day seafloor. In addition, the transition from aragonite to calcite typically preserves pseudomorphic fibers and rosettes of former aragonite (Treves and Harper, 1994), which were not observed in the present study. Therefore, an aragonite precursor is unlikely, and we concluded the type I carbonate was precipitated directly as calcite.

The Sr isotopic composition of carbonate can constrain its formation age by comparison with the Sr isotope ratios of seawater (Hart and Staudigel, 1986; Alt and Teagle, 2003; Kendrick et al., 2022). Some type I carbonate samples would retain the seawater Sr isotopic composition, but some samples would not, because the REE patterns of the type I carbonates vary from those typical of seawater to those typical of hydrothermal fluids (Fig. 9A). Key observations for assessing whether the carbonate retains an unmodified seawater signature are the comparison with the seawater $^{87}Sr/^{86}Sr$ values, and the REE patterns and $[\frac{Sr}{Ca}]_{Fluid}$ reconstructed from $[\frac{Sr}{Ca}]_{Calcite}$. In addition, carbonate Mn/Sr ratios (<3) can be used as a sensitive indicator of alteration, with a maximum Mn/Sr ratio in the range of 1–3 indicating unaltered Sr isotopic ratios (Kaufman et al., 1993; Jacobsen and Kaufman, 1999). The type I ophicarbonate KN22093012, KN22093014, KN23011006, and KN23011007 are unlikely to retain a seawater signature, because (i) their REE patterns show positive Eu anomalies (Fig. 9A) which suggest hydrothermal fluids were involved in the formation of the carbonates, (ii) the ophicarbonate KN23011006 and KN23011007 have elevated Mn/Sr ratio (3.6 and 3.4, respectively; Tables 2 and S1), and (iii) $^{87}Sr/^{86}Sr$ values of the ophicarbonate KN22093012 and KN22093014 (∼0.7063; Table 2) have not been observed for Phanerozoic seawater (Fig. 10A).

Contrary, the type I carbonates KN22072501 and KN22093004 likely retain their seawater signatures from the time of formation, because (i) they show pronounced negative Ce anomalies with no significant Eu anomalies, similar to the REE patterns of seawater (Fig. 9A), (ii) the $[\frac{Sr}{Ca}]_{Calcite}$ values of carbonate in the sample KN22072501 are 0.2–0.4 mmol/mol (Table S3), and the reconstructed $[\frac{Sr}{Ca}]_{Fluid}$at 120–160°C (3.7–10.5 mmol/mol) overlaps with the seawater [Sr/Ca] (Fig. S3), (iii) and the bulk Mn/Sr ratios of the carbonates are <3 (Table 2). Geochemical models of hydrothermal and seawater carbonate formation suggest that the Eu anomaly, rather than $^{87}Sr/^{86}Sr$, is sensitive to mixing with evolved hydrothermal fluids (Eickmann et al., 2009). Therefore, the absence of a significant Eu anomaly in carbonate in the ophicarbonates KN22072501 and KN22093004 suggests that they were formed from least modified seawater, possibly via a conductive heating mechanism proposed by Eickmann et al. (2009).

The $^{87}Sr/^{86}Sr$ values of sample KN22072501 are 0.707036–0.707082, within incertitude (Table 2). During the Phanerozoic, these carbonate $^{87}Sr/^{86}Sr$ ratios overlapped those of seawater during five time intervals (ca. 274–271, 254–252, 186–184, 169–167, and 149–148 Ma; Fig. 10A). Similarly, the $^{87}Sr/^{86}Sr$ values of sample KN22093004 (0.706869–0.706897, within incertitude) overlap those of seawater during four time intervals (ca. 270–264, 262–257, 164–163, and 154–153 Ma; Fig. 10A). These ages are prior to the accretion age of the Mikabu plateau (125–110 Ma; Sawada et al. 2019; Tominaga and Hara, 2021), suggesting that seawater (one of source fluids of the type I carbonate) was indeed available for alteration.

The timing of these intervals can be further refined by considering the tectonic context of the Mikabu Plateau. The pelagic sedimentary rocks, upon which the Mikabu Plateau was emplaced, contain Middle Jurassic radiolarians, suggesting a depositional period between 174 and 164 Ma (Sakakibara et al. 1993). Therefore, interactions prior to 174 Ma can be excluded. Moreover, our study (Supplementary text S1), along with previous research (Agata, 1994; Ozawa et al., 1997; Uesugi and Arai, 1999; Ichiyama et al., 2014), suggests that ultramafic rocks in the Mikabu unit were tectonically originated from intraplate setting. This implies that the carbonation of the ultramafic rocks must have occurred after intraplate magmatism (157–146 Ma; Ichiyama et al. 2018; Sawada et al. 2019; Tominaga and Hara, 2021) and after the crystallization of ultramafic cumulates during intraplate magmatism (153–142 Ma; Ozawa et al., 1997). Therefore, the $^{87}Sr/^{86}Sr$ ratios of carbonates from samples KN22072501 and

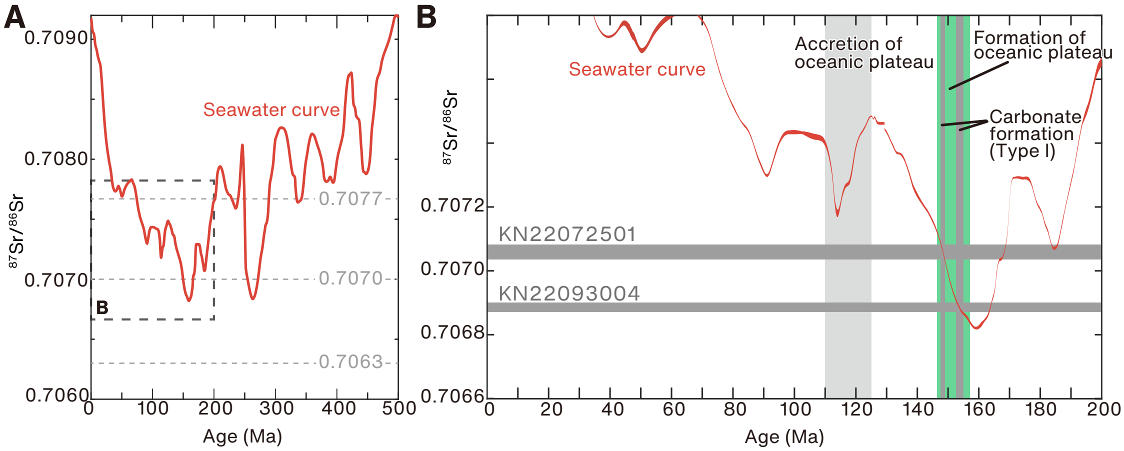

FIG. 10. (A) Phanerozoic seawater $^{87}Sr/^{86}Sr$ curve (red line) and representative $^{87}Sr/^{86}Sr$ values (gray dotted line) of carbonate. (B) $^{87}Sr/^{86}Sr$ ratios of carbonate (type I) and seawater. The seawater $^{87}Sr/^{86}Sr$ ratios are shown with the 95% confidence interval (McArthur et al., 2020) as a red band. The horizontal, dark gray area is the $^{87}Sr/^{86}Sr$ value $\pm 2\sigma$ for some type I carbonates (samples KN22072501 and KN22093004), which likely retain a seawater signature (see main text for details), and their intersection with the seawater $^{87}Sr/^{86}Sr$ curve represents the formation age of type I carbonate (vertical dark gray area; 149–148 Ma). The igneous and formation ages (157–146 Ma; vertical green area) of the oceanic plateau are from Ichiyama et al. (2018), Sawada et al. (2019), and Tominaga and Hara (2021). The accretion age (vertical light gray area; 125–110 Ma) is from Sawada et al. (2019) and Tominaga and Hara (2021).

KN22093004 most likely record interactions with seawater at ca. 149–148 and 154–153 Ma, respectively (Figs. 10B and 11A).

2. *Type II, III, and IV carbonates*

The type II, III, and IV carbonates have low $\delta^{13}C_{VPDB}$ values (-8.1‰ to -5.8‰), which are very different from the $\delta^{13}C_{VPDB}$ values of marine carbonates (Fig. 8A). The range of $\delta^{13}C_{VPDB}$ values is similar to that of metamorphic carbonates hosted in country metasediments of the Kanto Mountains (Fig. 8A), suggesting the carbon sources of type II, III, and IV carbonates were a mixture of organic ($\delta^{13}C_{VPDB}$ = -24.1‰ for the Mikabu metasediments; (Suzuki et al., 2017) and inorganic carbon (i.e., marine carbonates; $\delta^{13}C_{VPDB}$ = 0‰ ± 3‰; Ripperdan, 2001) released during devolatilization of metasedimentary rocks (Schwarzenbach et al., 2016; Menzel et al., 2018; Noël et al., 2018). A contribution from metasediments is also supported by the radiogenic $^{87}Sr/^{86}Sr$ ratios of the type II and IV carbonates (Fig. 8B), because sediments have radiogenic Sr (average $^{87}Sr/^{86}Sr \sim 0.7123$ for subducting sediments; Plank, 2014), and interactions with sediment-derived fluids would yield radiogenic Sr isotopic values (Yamaguchi et al., 2012; Cannaò et al., 2020).

A wide range of $\delta^{18}O_{VSMOW}$ values relative to the less-variable $\delta^{13}C_{VPDB}$ values for the type II, III, and IV carbonates (Fig. 8A) implies exchange with H_2O-rich fluid containing little or no carbon (depending on the temperature and $\delta^{18}O_{VSMOW}$ of the fluids), which was probably fluid derived from the dehydration of serpentinite (i.e., reaction such as serpentine + 3 $CO_{2(aq)}$ = 3 magnesite + 2 $SiO_{2(aq)}$ + 2 H_2O; e.g., Menzel et al. 2018). Because the $\delta^{18}O_{VSMOW}$ of the source fluid would be variable, the formation temperature of the type II, III, and IV carbonates cannot be estimated from the oxygen isotopic fractionation between carbonate and fluid. Fragments of dolomite crystals in the dolomite + calcite microbreccia in the type II (Fig. 7C) and IV (Fig. 7I) carbonate showed Mg-rich rims at the contact with calcite, suggesting such dolomite rims are in equilibrium with calcite. Using calcite–dolomite solvus thermometry (eq. 31 of Anovitz and Essene, 1987), minimum formation temperatures of the type II and IV carbonates yield temperatures of 266–397°C and 218–438°C, respectively (Table S6). These temperature estimates are similar to the peak metamorphic temperatures of the surrounding metapelites (300–360°C; Enami et al., 1994), considering the inherent error in the calibration of the calcite–dolomite solvus thermometry (±50°C; Anovitz and Essene, 1987). Thermodynamic models of the reaction between serpentinite and sediment-derived fluid have shown that dolomite is formed at a low fluid–rock ratio relative to calcite, because of variation of fluid Mg/Ca ratio (Okamoto et al., 2021; Leong et al., 2023), implying the occurrence of dolomite-rich carbonate (types II and IV) and calcite (type III) reflects variations in the fluid Mg/Ca ratio.

The type II, III, and IV carbonates would be formed from mixed carbon sources involving the devolatilization of metasediments containing organic and inorganic carbon. The supply of aqueous carbon sourced from the metasediments implies the ultramafic rocks were located near the metasediments. Moreover, the estimated temperatures from the type II and IV carbonates are similar to the peak temperatures of the metasediments. Therefore, the type II, III, and IV carbonates formed after accretion of the oceanic plateau (125–110 Ma; Sawada et al., 2019; Tominaga and Hara, 2021) at about the time of peak P–T metamorphism (ca. 90 Ma; Fig. 11B). This interpretation is also consistent with the occurrence of carbonate (Fig. 2D), which suggests that formation of type

III carbonate occurred after the formation of type I carbonate (which occurred in an oceanic setting). The type II and IV carbonates may have formed in mostly similar environments, although the type IV appears to have formed later than type II carbonate (Fig. 2B), based on the overall similarity of geochemical characteristics (REE, C-O-Sr isotopes, and temperature estimates) between these carbonates.

B. Implications

The present study indicates that carbonates in the type I ophicarbonates formed in the oceanic stage before subduction (Fig. 11A), while the carbonates in the type II, III, and IV ophicarbonates formed after accretion of the oceanic plateau (Fig. 11B). The timing of carbonate formation in the type I ophicarbonate was most likely 154–148 Ma, which is similar to the age of the igneous protoliths of the Mikabu unit (157–146 Ma; Ichiyama et al., 2018; Sawada et al., 2019; Tominaga and Hara, 2021; Fig. 10B). In the modern oceanic plateaux, the occurrence of hydrothermal alteration has been attributed to the magmatic activity during its formation (Li et al., 2014; Beier et al., 2019). Moreover, presence of serpentinized layer has been inferred around the Moho beneath seamounts based on observations of serpentinized xenoliths from the Kerguelen oceanic plateau (Wasilewski et al., 2017; Cortiade et al., 2022), geophysical observations of anisotropic and low-velocity layer at the Hawaii and the Azores seamounts (Park and Rye, 2019a, b), and heterogeneous earthquake distributions in the subducted oceanic mantle (Geersen et al., 2022). Park and Rye (2019a, b) suggested that serpentinization of ultramafic rock beneath seamounts is possible because (i) thermal cracking (Korenaga, 2007, 2017) due to magmatism and/or thermal rejuvenation creates a fracture network near volcanic centers to promote fluid infiltration, and (ii) subsequent reaction-driven fracturing during serpentinization (Jamtveit et al., 2008; Malvoisin et al., 2017; Yoshida et al., 2020; Uno et al., 2022) and flexural stresses induced by volcanic loading (Hieronymus and Bercovici, 2001; Richards et al., 2013) create new fractures that allow continuous fluid infiltration. The present study suggests that the hydrothermal activity, most likely associated with formation of an oceanic plateau, can cause substantial geochemical modification by the interaction between oceanic serpentinite and circulating seawater.

In the possible scenario, the similarity between the timing of carbonation (type I carbonate) and emplacement of an oceanic plateau suggests that alteration of an oceanic plateau occurs rapidly after its emplacement (Figs. 10B and 11A). Such rapid hydrothermal alteration has been observed for modern oceanic plateaux. For example, Beier et al. (2019) investigated the submarine Azores Plateau (formed at ca. 10 Ma) in the central North Atlantic and suggested that significant mass transfer and hydrothermal alteration (including carbonate formation) of the oceanic plateau were induced by magmatic activity during plateau formation. They proposed that hydrothermal alteration occurs on geologically rapid timescales ($<$10 Myr), based on the presence of hydrothermal alteration in young rocks (ca. 10 Ma). Similarly, Li et al. (2014) suggested that carbonate formation from hydrothermal fluids at the Shatsky Rise in the Pacific Ocean occurs within a few million years of the emplacement of an oceanic plateau. These observations of rapid carbonate formation suggest that oceanic plateaux respond rapidly (¡10 Myr) to perturbations of carbon outflux induced by intraplate magmatism during oceanic plate emplacement and sequester their own carbon emissions. This negative feedback on carbon cycling may be analogous to the rapid rock weathering and carbon sequestration induced by carbon outflux from continental LIPs (Dessert et al., 2003; Schaller et al., 2012; Johansson et al., 2018).

Using the densities of serpentine (2.60 g $\mathrm{cm^{-3}}$) and calcite (2.71 g $\mathrm{cm^{-3}}$), and the C concentration in calcite (12 wt.%), we can estimate that the bulk ophicarbonate (composed of equal volumetric amounts of serpentine and calcite) contains 163 kg $\mathrm{m^{-3}}$ of carbon. Using the approximate thickness of ophicarbonate layer in the Kanasaki serpentinites (Fig. 1D, E), we infer that a 10–100 m thick ophicarbonate layer is present beneath the modern oceanic plateau. The total area of the modern oceanic plateaus is 1.8×10^{13} $\mathrm{m^3}$ (Harris et al., 2014). If the hydrothermally affected area beneath the modern constitutes 0.1–1% of the total area, we can estimate the carbon reservoir potential of ophicarbonate beneath the modern oceanic plateau to be $0.003 - 3.0 \times 10^6$ Mt C globally. This estimate is 0.001–0.077% of the carbon reservoir size of the carbonated oceanic crust (3.9×10^9 Mt C; Hirschmann, 2018), although it contains high uncertainty derived from the assumption of the extent of the hydrothermal alteration. Further research is needed to fully assess the impact of ophicarbonate on the geological carbon cycle.

Our study suggests that the type II, III, and IV carbonates were formed by reaction with fluid derived from metasediments during greenschist-faces metamorphism after accretion of the oceanic plateau. Such a mechanism of carbonation is similar to that observed at the subduction interface, where fluids derived from subducting sediments infiltrate the forearc mantle wedge (Scambelluri et al., 2016; Peng et al., 2020; Okamoto et al., 2021; Kelemen et al., 2022; Leong et al., 2023). However, unlike subduction interfaces, the accretion and subsequent peeling-off of the oceanic plateau is required for the basal layer of the oceanic plateau to be entrapped by subducting sediments. Our present study suggests that oceanic plateau accretion and subsequent sediment underplating is an important process that can drive further carbonate formation in the accreted margins. Moreover, carbonate in accreted oceanic plateaux may serve as a long-term carbon reservoir. In general, subduction of altered basaltic oceanic crust (formed primarily at a mid-ocean ridge) would recycle carbon to the surface through processes such as metamorphic devolatilization and arc volcanism (Arzilli et al., 2023). Such a cycle of carbon in the oceanic crust can take place on the order of tens of Myr after its subduction (Galvez and Pubellier, 2019; Horton, 2021). In contrast, oceanic plateaux are more likely to accrete on island arcs and active continental margins than be subducted, because they are much more buoyant than basaltic oceanic crust (e.g., Kerr, 2014). As a result, carbon

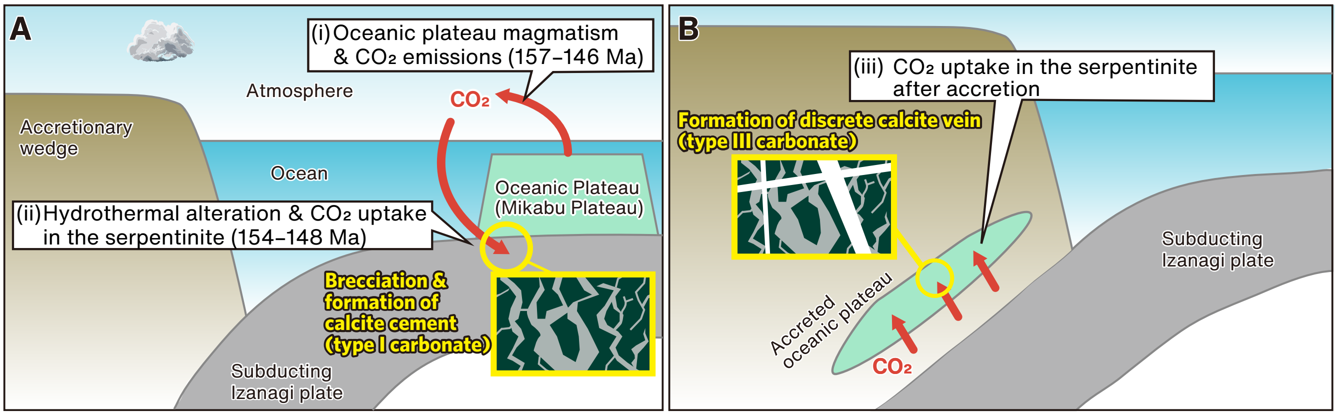

FIG. 11. Schematic model of serpentinite carbonation and carbon cycling associated with extensive intraplate magmatism. Formation of the type I and III carbonates is shown. (A) Formation of ophicarbonate with type I carbonate at 154–148 Ma. (B) After accretion of the oceanic plateau (125–110 Ma), the discrete calcite veins (type III carbonate) formed, likely at peak metamorphic conditions (ca. 90 Ma). Other carbonates (types II and IV) formed in the accretionary wedge, similar to type III carbonate (see text for details).

stored in the accreted oceanic plateaux would not be released by metamorphic devolatilization and is likely to persist without being recycled, leading to a longer residence time for carbonate in these settings. Barry et al. (2019) proposed that a significant amount of carbon is sequestered as carbonate in the forearc crust. Since accreted oceanic plateaux are difficult to detect (Dilek and Ernst, 2008), the forearc carbon reservoir could be hosted by accreted oceanic plateaux.

Overall, the present study found that carbon uptake in the oceanic serpentinite would occur during and after the emplacement of oceanic plateaus, highlighting the potential importance of the life cycle of the oceanic plateaus (from emplacement to accretion) in the global carbon cycle. The oceanic plateaus have been forming throughout much of the Earth's history (e.g., Kerr, 2014). The present study implies that negative feedback in the geological carbon cycle, consisting of carbon release during the oceanic plateau emplacement, subsequent alteration, and carbon uptake, may have modulated atmospheric CO_2 and the Earth's surface environments throughout its history.

VI. CONCLUSION

This study investigated carbonated serpentinites (ophicarbonates) that occur with mafic meta-volcanic rocks, which were part of an oceanic plateau in the Late Jurassic Paleo-Pacific Ocean. Our main findings are as follows.

1. Four types of carbonates were observed in the ophicarbonates: calcite cement in brecciated serpentinite (type I), dolomite + calcite cement in brecciated serpentinite (type II), discrete calcite veins in serpentinite (type III), and discrete dolomite + calcite veins in serpentinite (type IV).

2. C–O–Sr isotope and trace element data constrained the source of the fluids that induced carbonation. The calcite cement (type I) formed in an oceanic setting by mixing of seawater and hydrothermal fluids before accretion, most likely at 154–148 Ma. Hydrothermal alteration and carbonation of ultramafic cumulates in an oceanic setting occurred in a hydrothermal system, most likely driven by extensive volcanism that formed a Late Jurassic oceanic plateau. In this possible scenario, the alteration of the oceanic plateau occurred rapidly after its emplacement (<10 Myr), and carbon uptake by hydrothermal alteration of an oceanic plateau can quickly sequester carbon emissions from the plateau.

3. The dolomite + calcite cement (type II), discrete calcite veins (type III), and discrete dolomite + calcite veins (type IV) formed in a subduction zone from CO_2-rich fluids sourced by the devolatilization of metasediments, likely after accretion of the oceanic plateau (125–110 Ma). Accretion and peeling-off of the oceanic plateau is required for the basal layer of the oceanic plateau to be entrapped by subducting sediments. Therefore, our present study suggests that oceanic plateau accretion, peeling-off of the basal layer of the oceanic plateau, and subsequent sediment underplating drive carbonate formation in the accreted margins. Compared to the oceanic crust, oceanic plateaux are difficult to subduct, suggesting accreted oceanic plateaux may be a stable reservoir of carbon over geologic time.

4. Carbon uptake in the oceanic serpentinite would occur during and after the emplacement of oceanic plateaus. A negative feedback in the geological carbon cycle, involving carbon release during the oceanic plateau emplacement, subsequent alteration, and carbon uptake, may have modulated atmospheric CO_2 and Earth's surface environments.

ACKNOWLEDGMENTS

We thank Mitsuhiro Toriumi, Mutsuko Inui, Tatsuya Miyata, and Kohei Hatakeyama for help with the fieldwork. Mayuko Fukuyama, Masakazu Fujii, and Otgonbayar Dandar are thanked for useful discussions. We thank Mike Lott for C–O isotope analysis at Washington State University, and Rikako Nohara for the assistance in trace element and Sr isotope analysis at Niigata University. Comments from three anonymous reviewers improved the earlier version of manuscript. We are grateful for constructive reviews from Rémi Coltat and an anonymous reviewer, as well as editorial handling by Mihai Ducea and Antoine Triantafyllou. This research was supported by the Japan Society for the Promotion of Science KAKENHI grants (JP22H04932, JP23K13198, JP23KJ2220, and JP23K13194) and an Earthquake Research Institute (The University of Tokyo) joint research program (ERI JURP 2024-B-01).

REFERENCES CITED

Agata, T., 1994, The Asama igneous complex, central Japan: An ultramafic-mafic layered intrusion in the Mikabu greenstone belt, Sambagawa metamorphic terrain: Lithos, v. 33, p. 241–263, doi:10.1016/0024-4937(94)90032-9.

Alt, J.C., and Teagle, D.A.H., 2003, Hydrothermal alteration of upper oceanic crust formed at a fast-spreading ridge: Mineral, chemical, and isotopic evidence from ODP Site 801: Chemical Geology, v. 201, p. 191–211, doi:10.1016/S0009-2541(03)00201-8.

Anovitz, L.M., and Essene, E.J., 1987, Phase Equilibria in the System CaCO3-MgCO3-FeCO3: Journal of Petrology, v. 28, p. 389–415, doi:10.1093/petrology/28.2.389.

Aoya, M., Endo, S., Mizukami, T., and Wallis, S.R., 2013, Paleo-mantle wedge preserved in the Sambagawa high-pressure: Metamorphic belt and the thickness of forearc continental crust: Geology, v. 41, p. 451–454, doi:10.1130/G33834.1.

Arzilli, F., Burton, M., La Spina, G., Macpherson, C.G., van Keken, P.E., and McCann, J., 2023, Decarbonation of subducting carbonate-bearing sediments and basalts of altered oceanic crust: Insights into recycling of CO2 through volcanic arcs: Earth and Planetary Science Letters, v. 602, p. 117945, doi:10.1016/j.epsl.2022.117945.

Bach, W., Rosner, M., Jöns, N., Rausch, S., Robinson, L.F., Paulick, H., and Erzinger, J., 2011, Carbonate veins trace seawater circulation during exhumation and uplift of mantle rock: Results from ODP Leg 209: Earth and Planetary Science Letters, v. 311, p. 242–252, doi:10.1016/j.epsl.2011.09.021.

Banno, S., 2004, Ultramafic Rocks and Associated Eclogites of the Sanbagawa Schists, Japan: A Review: International Geology Review, v. 46, p. 693–704, doi:10.2747/0020-6814.46.8.693.

Barry, P.H. et al., 2019, Forearc carbon sink reduces long-term volatile recycling into the mantle: Nature, v. 568, p. 487–492, doi:10.1038/s41586-019-1131-5.

Beier, C., Bach, W., Busch, A. V., Genske, F.S., Hübscher, C., and Krumm, S.H., 2019, Extreme intensity of fluid-rock interaction during extensive intraplate volcanism: Geochimica et Cosmochimica Acta, v. 257, p. 26–48, doi:10.1016/j.gca.2019.04.017.

Bernoulli, D., and Weissert, H., 2021a, Oxygen isotopes in ophicalcites: an ever-lasting controversy? International Journal of Earth Sciences, v. 110, p. 1–8, doi:10.1007/s00531-020-01934-5.

Bernoulli, D., and Weissert, H., 2021b, Reply to 'Discussion of oxygen isotopes in ophicalcites: an ever-lasting controversy?' by R. Coltat, Ph. Boulvais, Y. Branquet, M. Poujol, P. Gautier and G. Manatschal: International Journal of Earth Sciences, v. 110, p. 1123–1125, doi:10.1007/s00531-021-01985-2.

Black, B.A., and Gibson, S.A., 2019, Deep carbon and the life cycle of large igneous provinces: Elements, v. 15, p. 319–324, doi:10.2138/gselements.15.5.319.

Burton, M.R., Sawyer, G.M., and Granieri, D., 2013, Deep carbon emissions from volcanoes: Reviews in Mineralogy and Geochemistry, v. 75, p. 323–354, doi:10.2138/rmg.2013.75.11.

Cannaò, E., Scambelluri, M., Bebout, G.E., Agostini, S., Pettke, T., Godard, M., and Crispini, L., 2020, Ophicarbonate evolution from seafloor to subduction and implications for deep-Earth C cycling: Chemical Geology, v. 546, p. 119626, doi:10.1016/j.chemgeo.2020.119626.

Coffin, M.F., and Eldholm, O., 1994, Large igneous provinces: Crustal structure, dimensions, and external consequences: Reviews of Geophysics, v. 32, p. 1–36, doi:10.1029/93RG02508.

Coltat, R., Boulvais, P., Branquet, Y., Collot, J., Epin, M.E., and Manatschal, G., 2019, Syntectonic carbonation during synmagmatic mantle exhumation at an ocean-continent transition: Geology, v. 47, p. 183–186, doi:10.1130/G45530.1.

Coltat, R., Boulvais, P., Branquet, Y., Poujol, M., Gautier, P., and Manatschal, G., 2021, Discussion to "Oxygen isotope in ophicalcites: an ever-lasting controversy?" International Journal of Earth Sciences, v. 110, p. 1117–1121, doi:10.1007/s00531-021-01983-4.

Coltorti, M., Bonadiman, C., Faccini, B., Grégoire, M., O'Reilly, S.Y., and Powell, W., 2007, Amphiboles from suprasubduction and intraplate lithospheric mantle: Lithos, v. 99, p. 68–84, doi:10.1016/j.lithos.2007.05.009.

Cortiade, N., Delacour, A., Guillaume, D., Moine, B., and Chevet, J., 2022, Serpentinization of mantle xenoliths in Kerguelen archipelago: A first petrographic and geochemical study: Lithos, v. 428–429, doi:10.1016/j.lithos.2022.106796.

Daëron, M., Drysdale, R.N., Peral, M., Huyghe, D., Blamart, D., Coplen, T.B., Lartaud, F., and Zanchetta, G., 2019, Most Earth-surface calcites precipitate out of isotopic equilibrium: Nature Communications, v. 10, p. 1–7, doi:10.1038/s41467-019-08336-5.

Dessert, C., Dupré, B., Gaillardet, J., François, L.M., and Allègre, C.J., 2003, Basalt weathering laws and the impact of basalt weathering on the global carbon cycle: Chemical Geology, v. 202, p. 257–273, doi:10.1016/j.chemgeo.2002.10.001.

Dilek, Y., and Ernst, R., 2008, Links between ophiolites and Large Igneous Provinces (LIPs) in Earth history: Introduction: Lithos, v. 100, p. 1–13, doi:10.1016/j.lithos.2007.08.001.

Eickmann, B., Bach, W., Rosner, M., and Peckmann, J., 2009, Geochemical constraints on the modes of carbonate precipitation in peridotites from the

Logatchev Hydrothermal Vent Field and Gakkel Ridge: Chemical Geology, v. 268, p. 97–106, doi:10.1016/j.chemgeo.2009.08.002.

Elderfield, H., 1988, The oceanic chemistry of the rare-earth elements: Philosophical Transactions of the Royal Society of London. Series A, Mathematical and Physical Sciences, v. 325, p. 105–126, doi:10.1098/rsta.1988.0046.

Enami, M., 1983, Petrology of pelitic schists in the oligoclase-biotite zone of the Sanbagawa metamorphic terrain, Japan: phase equilibria in the highest grade zone of a high-pressure intermediate type of metamorphic belt: Journal of Metamorphic Geology, v. 1, p. 141–161, doi:10.1111/j.1525-1314.1983.tb00269.x.

Enami, M., Wallis, S.R., and Banno, Y., 1994, Paragenesis of sodic pyroxene-bearing quartz schists: implications for the P-T history of the Sanbagawa belt: Contributions to Mineralogy and Petrology, v. 116, p. 182–198, doi:10.1007/BF00310699.

Endo, S., Kouketsu, Y., and Aoya, M., 2024, Sanbagawa Subduction: What Went in, How Deep, and How Hot did it Get? Elements, v. 20, p. 77–82, doi:10.2138/gselements.20.2.77.

Endo, S., Wallis, S., Hirata, T., Anczkiewics, R., Platt, J., Thirlwall, M., and Asahara, Y., 2009, Age and early metamorphic history of the Sanbagawa belt: Lu-Hf and P - T constraints from the Western Iratsu eclogite: Journal of Metamorphic Geology, v. 27, p. 371–384, doi:10.1111/j.1525-1314.2009.00821.x.

Ernst, R.E., Bond, D.P.G., Zhang, S., Buchan, K.L., Grasby, S.E., Youbi, N., El Bilali, H., Bekker, A., and Doucet, L.S., 2021, Large Igneous Province Record Through Time and Implications for Secular Environmental Changes and Geological Time-Scale Boundaries, *in* Large Igneous Provinces: A Driver of Global Environmental and Biotic Changes, p. 1–26, doi:10.1002/9781119507444.ch1.

Faure, G., and Mensing, T.M., 2004, Isotopes: Principles and Applications (3rd Edition, Ed.): Wiley, 928 p.

Früh-Green, G.L., Kelley, D.S., Bernasconi, S.M., Karson, J.A., Ludwig, K.A., Butterfield, D.A., Boschi, C., and Proskurowski, G., 2003, 30,000 Years of hydrothermal activity at the Lost City vent field: Science, doi:10.1126/science.1085582.

Früh-Green, G.L., Weissert, H., and Bernoulli, D., 1990, A multiple fluid history recorded in Alpine ophiolites: Journal of the Geological Society, v. 147, p. 959–970, doi:10.1144/gsjgs.147.6.0959.

Galvez, M.E., and Pubellier, M., 2019, How Do Subduction Zones Regulate the Carbon Cycle?, *in* Deep Carbon, Cambridge University Press, p. 276–312, doi:10.1017/9781108677950.010.

Geersen, J., Sippl, C., and Harmon, N., 2022, Impact of bending-related faulting and oceanic-plate topography on slab hydration and intermediate-depth seismicity: Geosphere, v. 18, p. 562–584, doi:10.1130/GES02367.1.

German, C.R., and Elderfield, H., 1990, Application of the Ce anomaly as a paleoredox indicator: The ground rules: Paleoceanography, v. 5, p. 823–833, doi:10.1029/PA005i005p00823.

Hara, H., Mori, H., Tominaga, K., and Nobe, Y., 2021, Progressive low-grade metamorphism reconstructed from the raman spectroscopy of carbonaceous material and an EBSD analysis of quartz in the sanbagawa metamorphic event, central Japan: Minerals, v. 11, doi:10.3390/min11080854.

Harris, P.T., Macmillan-Lawler, M., Rupp, J., and Baker, E.K., 2014, Geomorphology of the oceans: Marine Geology, v. 352, p. 4–24, doi:10.1016/j.margeo.2014.01.011.

Hart, S.R., and Staudigel, H., 1986, Ocean crust vein mineral deposition: Rb Sr ages, U-Th-Pb geochemistry, and duration of circulation at DSDP sites 261, 462 and 516: Geochimica et Cosmochimica Acta, v. 50, p. 2751–2761, doi:10.1016/0016-7037(86)90224-3.

Hashimoto, M., Tagiri, M., Kusakabe, K., Masuda, K., and Yano, T., 1992, Geologic structure formed by tectonic stacking of sliced layers in the Sanbagawa metamorphic terrain, Kodama-Nagatoro area, Kanto Mountains.: The Journal of the Geological Society of Japan, v. 98, p. 953–965, doi:10.5575/geosoc.98.953.

Hastie, A.R., and Kerr, A.C., 2010, Mantle plume or slab window?: Physical and geochemical constraints on the origin of the Caribbean oceanic plateau: Earth-Science Reviews, v. 98, p. 283–293, doi:10.1016/j.earscirev.2009.11.001.

Hattori, K., Wallis, S., Enami, M., and Mizukami, T., 2010, Subduction of mantle wedge peridotites: Evidence from the Higashi-akaishi ultramafic body in the Sanbagawa metamorphic belt: Island Arc, v. 19, p. 192–207, doi:10.1111/j.1440-1738.2009.00696.x.

Heydolph, K., Murphy, D.T., Geldmacher, J., Romanova, I. V., Greene, A., Hoernle, K., Weis, D., and Mahoney, J., 2014, Plume versus plate origin for the Shatsky Rise oceanic plateau (NW Pacific): Insights from Nd, Pb and Hf isotopes: Lithos, v. 200–201, p. 49–63, doi:10.1016/j.lithos.2014.03.031.

Hieronymus, C.F., and Bercovici, D., 2001, A theoretical model of hotspot volcanism: Control on volcanic spacing and patterns via magma dynamics and lithospheric stresses: Journal of Geophysical Research: Solid Earth, v. 106, p. 683–702, doi:10.1029/2000jb900355.

Hirauchi, K. ichi, Nagata, Y., Kataoka, K., Oyanagi, R., Okamoto, A., and Michibayashi, K., 2021, Cataclastic and crystal-plastic deformation in shallow mantle-wedge serpentinite controlled by cyclic changes in pore fluid pressures: Earth and

Planetary Science Letters, v. 576, p. 117232, doi:10.1016/j.epsl.2021.117232.

Hirschmann, M.M., 2018, Comparative deep Earth volatile cycles: The case for C recycling from exosphere/mantle fractionation of major (H2O, C, N) volatiles and from H2O/Ce, CO2/Ba, and CO2/Nb exosphere ratios: Earth and Planetary Science Letters, v. 502, p. 262–273, doi:10.1016/j.epsl.2018.08.023.

Hisada, K., Nakazawa, E., and Arai, S., 1993, Sedimentary origon of ophicalcite in the Sambagawa metamorphic rocks, Kanto Mountains, central Japan: Annual report of the Institute of Geoscience, the University of Tsukuba, v. 19, p. 43–47.

Horton, F., 2021, Rapid recycling of subducted sedimentary carbon revealed by Afghanistan carbonatite volcano: Nature Geoscience, v. 14, p. 508–512, doi:10.1038/s41561-021-00764-7.

Ichiyama, Y., Ishiwatari, A., Kimura, J.I., Senda, R., and Miyamoto, T., 2014, Jurassic plume-origin ophiolites in Japan: Accreted fragments of oceanic plateaus: Contributions to Mineralogy and Petrology, v. 168, p. 1–24, doi:10.1007/s00410-014-1019-1.

Ichiyama, Y., Takahashi, S., and Ito, H., 2018, Zircon U-Pb ages of the Mikabu ophiolitic belt, Southwest Japan: Implications for the origin of the Shatsky Rise, *in* EGU General Assembly Conference Abstracts, v. 20, p. 11879, https://meetingorganizer.copernicus.org/EGU2018/EGU2018-11879.pdf.

Inomata, M., and Tazaki, K., 1974, Phlogopite and Ti-pargasite-bearing ultramafic rocks from the Mikabu zone, Central Japan: The Journal of the Japanese Association of Mineralogists, Petrologists and Economic Geologists, v. 69, p. 205–214, doi:10.2465/ganko1941.69.205.

Ishiwatari, A., Ozawa, K., Arai, S., Ishimaru, S., Abe, N., and Takeuchi, M., 2016, Ophiolites and ultramafic rocks, *in* The Geology of Japan, Geological Society London, p. 223–250, doi:10.1144/GOJ.9.

Isozaki, Y., Maruyama, S., and Furuoka, F., 1990, Accreted oceanic materials in Japan: Tectonophysics, v. 181, p. 179–205, doi:10.1016/0040-1951(90)90016-2.

Jacobsen, S.B., and Kaufman, A.J., 1999, The Sr, C and O isotopic evolution of Neoproterozoic seawater: Chemical Geology, v. 161, p. 37–57, doi:10.1016/S0009-2541(99)00080-7.

Jamtveit, B., Malthe-Sørenssen, A., and Kostenko, O., 2008, Reaction enhanced permeability during retrogressive metamorphism: Earth and Planetary Science Letters, v. 267, p. 620–627, doi:10.1016/j.epsl.2007.12.016.

Jiang, Q., Jourdan, F., Olierook, H.K.H., Merle, R.E., Bourdet, J., Fougerouse, D., Godel, B., and Walker, A.T., 2022, Volume and rate of volcanic CO2 emissions governed the severity of past environmental crises: Proceedings of the National Academy of Sciences of the United States of America, v. 119, p. 1–10, doi:10.1073/pnas.2202039119.

Jochum, K.P., Willbold, M., Raczek, I., Stoll, B., and Herwig, K., 2005, Chemical Characterisation of the USGS Reference Glasses GSA-1G, GSC-1G, GSD-1G, GSE-1G, BCR-2G, BHVO-2G and BIR-1G Using EPMA, ID-TIMS, ID-ICP-MS and LA-ICP-MS: Geostandards and Geoanalytical Research, v. 29, p. 285–302, doi:10.1111/j.1751-908X.2005.tb00901.x.

Johansson, L., Zahirovic, S., and Müller, R.D., 2018, The Interplay Between the Eruption and Weathering of Large Igneous Provinces and the Deep-Time Carbon Cycle: Geophysical Research Letters, v. 45, p. 5380–5389, doi:10.1029/2017GL076691.

Jones, M.T., Jerram, D.A., Svensen, H.H., and Grove, C., 2016, The effects of large igneous provinces on the global carbon and sulphur cycles: Palaeogeography, Palaeoclimatology, Palaeoecology, v. 441, p. 4–21, doi:10.1016/j.palaeo.2015.06.042.

Kaufman, A.J., Jacobsen, S.B., and Knoll, A.H., 1993, The Vendian record of Sr and C isotopic variations in seawater: Implications for tectonics and paleoclimate: Earth and Planetary Science Letters, v. 120, p. 409–430, doi:10.1016/0012-821X(93)90254-7.

Kelemen, P.B. et al., 2022, Listvenite Formation During Mass Transfer into the Leading Edge of the Mantle Wedge: Initial Results from Oman Drilling Project Hole BT1B: Journal of Geophysical Research: Solid Earth, v. 127, p. 1–38, doi:10.1029/2021jb022352.

Kelemen, P.B., and Manning, C.E., 2015, Reevaluating carbon fluxes in subduction zones, what goes down, mostly comes up: Proceedings of the National Academy of Sciences, v. 112, p. E3997–E4006, doi:10.1073/pnas.1507889112.

Kendrick, M.A., Zhao, J., and Feng, Y., 2022, Early accretion and prolonged carbonation of the Pacific Ocean's oldest crust: Geology, v. 50, p. 1270–1275, doi:10.1130/G49985.1.

Kerr, A.C., 2014, Oceanic Plateaus, *in* Treatise on Geochemistry, Elsevier, v. 4, p. 631–667, doi:10.1016/B978-0-08-095975-7.00320-X.

Kerr, A.C., Tarney, J., Nivia, A., Marriner, G.F., and Saunders, A.D., 1998, The internal structure of oceanic plateaus: Inferences from obducted Cretaceous terranes in western Colombia and the Caribbean: Tectonophysics, v. 292, p. 173–188, doi:10.1016/S0040-1951(98)00067-5.

Kerr, A.C., White, R. V., and Saunders, A.D., 2000, LIP Reading: Recognizing Oceanic Plateaux in the Geological Record: Journal of Petrology, v. 41, p. 1041–1056, doi:10.1093/petrology/41.7.1041.

Kim, S.T., and O'Neil, J.R., 1997, Equilibrium and nonequilibrium oxygen isotope effects in synthetic carbonates: Geochimica et Cosmochimica Acta, v. 61, p. 3461–3475, doi:10.1016/S0016-7037(97)00169-5.

Kimura, J.I., and Chang, Q., 2012, Origin of the suppressed matrix effect for improved analytical performance in determination of major and trace elements in anhydrous silicate samples using 200 nm femtosecond laser ablation sector-field inductively coupled plasma mass spectrometry: Journal of Analytical Atomic Spectrometry, v. 27, p. 1549–1559, doi:10.1039/c2ja10344c.

Kimura, G., Sakakibara, M., and Okamura, M., 1994, Plumes in central Panthalassa? Deductions from accreted oceanic fragments in Japan: Tectonics, v. 13, p. 905–916, doi:10.1029/94TC00351.

Klein, F., Schroeder, T., John, C.M., Davis, S., Humphris, S.E., Seewald, J.S., Sichel, S., Bach, W., and Brunelli, D., 2024, Mineral carbonation of peridotite fueled by magmatic degassing and melt impregnation in an oceanic transform fault: Proceedings of the National Academy of Sciences, v. 121, p. 2017, doi:10.1073/pnas.2315662121.

Klinkhammer, G.P., Elderfield, H., Edmond, J.M., and Mitra, A., 1994, Geochemical implications of rare earth element patterns in hydrothermal fluids from mid-ocean ridges: Geochimica et Cosmochimica Acta, v. 58, p. 5105–5113, doi:10.1016/0016-7037(94)90297-6.

Korenaga, J., 2017, On the extent of mantle hydration caused by plate bending: Earth and Planetary Science Letters, v. 457, p. 1–9, doi:10.1016/j.epsl.2016.10.011.

Korenaga, J., 2007, Thermal cracking and the deep hydration of oceanic lithosphere: A key to the generation of plate tectonics? Journal of Geophysical Research: Solid Earth, v. 112, doi:10.1029/2006JB004502.

Koto, B., 1888, On the so-called Crystalline Schists of Chichibu (The Sambagawan Series): The journal of the College of Science, Imperial University, Japan, p. 77–141.

Kouketsu, Y., Enami, M., Mouri, T., Okamura, M., and Sakurai, T., 2014, Composite metamorphic history recorded in garnet porphyroblasts of Sambagawa metasediments in the Besshi region, central Shikoku, Southwest Japan: Island Arc, v. 23, p. 263–280, doi:10.1111/iar.12075.

Kunugiza, K., Takasu, A., and Banno, S., 1986, The origin and metamorphic history of the ultramafic and metagabbro bodies in the Sanbagawa metamorphic belt: Memoir of the Geological Society of America, v. 164, p. 375–385, doi:10.1130/MEM164-p375.

Labotka, T.C., Cole, D.R., and Riciputi, L.R., 2000, Diffusion of C and O in calcite at 100 MPa: American Mineralogist, v. 85, p. 488–494, doi:10.2138/am-2000-0410.

Lawrence, M.G., Greig, A., Collerson, K.D., and Kamber, B.S., 2006, Rare earth element and yttrium variability in South East Queensland waterways: Aquatic Geochemistry, v. 12, p. 39–72, doi:10.1007/s10498-005-4471-8.

Leake, B.E. et al., 1997, Nomenclature of Amphiboles; Report of the Subcommittee on Amphiboles of the International Mineralogical Association Commission on New Minerals and Mineral Names: Mineralogical Magazine, v. 61, p. 295–310, doi:10.1180/minmag.1997.061.405.13.

Leong, J.A., de Obeso, J.C., Manning, C.E., and Kelemen, P.B., 2023, Thermodynamic constraints on the fate of carbon mobilized from subducted sediments in the overlying mantle wedge: Earth and Planetary Science Letters, v. 623, p. 118424, doi:10.1016/j.epsl.2023.118424.

Li, S., Geldmacher, J., Hauff, F., Garbe-Schönberg, D., Yu, S., Zhao, S., and Rausch, S., 2014, Composition and timing of carbonate vein precipitation within the igneous basement of the Early Cretaceous Shatsky Rise, NW Pacific: Marine Geology, v. 357, p. 321–333, doi:10.1016/j.margeo.2014.09.046.

Makimoto, H., and Takeuchi, K., 1992, Geology of the Yorii district.: Geological Survey of Japan, 136 p.

Malvoisin, B., Brantut, N., and Kaczmarek, M.A., 2017, Control of serpentinisation rate by reaction-induced cracking: Earth and Planetary Science Letters, v. 476, p. 143–152, doi:10.1016/j.epsl.2017.07.042.

McArthur, J.M., Howarth, R.J., Shields, G.A., and Zhou, Y., 2020, Strontium Isotope Stratigraphy: Geologic Time Scale 2020, p. 211–238, doi:10.1016/B978-0-12-824360-2.00007-3.

McCollom, T.M., 2008, Observational, experimental, and theoretical constraints on carbon cycling in mid-ocean ridge hydrothermal systems: Geophysical Monograph Series, v. 178, p. 193–213, doi:10.1029/178GM10.

Menzel, M.D., Garrido, C.J., López Sánchez-Vizcaíno, V., Marchesi, C., Hidas, K., Escayola, M.P., and Delgado Huertas, A., 2018, Carbonation of mantle peridotite by CO2-rich fluids: the formation of listvenites in the Advocate ophiolite complex (Newfoundland, Canada): Lithos, v. 323, p. 238–261, doi:10.1016/j.lithos.2018.06.001.

Menzel, M.D., Sieber, M.J., and Godard, M., 2024, From peridotite to listvenite – perspectives on the processes, mechanisms and settings of ultramafic mineral carbonation to quartz-magnesite rocks: Earth-Science Reviews, v. 255, p. 104828, doi:10.1016/j.earscirev.2024.104828.

Miyazaki, T., and Shuto, K., 1998, Sr and Nd isotope ratios of twelve GSJ rock reference samples: Geochemical Journal, v. 32, p. 345–350, doi:10.2343/geochemj.32.345.

Mizukami, T., Yokoyama, H., Hiramatsu, Y., Arai, S., Kawahara, H., Nagaya, T., and Wallis, S.R., 2014, Two types of antigorite serpentinite controlling heterogeneous slow-slip behaviours of slab-mantle interface: Earth and Planetary Science Letters, v. 401, p. 148–158, doi:10.1016/j.epsl.2014.06.009.

Morohashi, K., Okamoto, A., Satish-Kumar, M., and Tsuchiya, N., 2008, Variations in stable isotope compositions (δ13C, δ18O) of calcite within exhumation-related veins from the Sanbagawa metamorphic belt: Journal of Mineralogical and Petrological Sciences, v. 103, p. 361–364, doi:10.2465/jmps.080620b.

Müller, R.D., Mather, B., Dutkiewicz, A., Keller, T., Merdith, A., Gonzalez, C.M., Gorczyk, W., and Zahirovic, S., 2022, Evolution of Earth's tectonic carbon conveyor belt: Nature, v. 605, p. 629–639, doi:10.1038/s41586-022-04420-x.

Neo, N., Yamazaki, S., and Miyashita, S., 2009, Data report: bulk rock compositions of samples from the IODP Expedition 309/312 sample pool, ODP Hole 1256D, *in* Proceedings of the IODP, 309/312, Integrated Ocean Drilling Program, v. 309, doi:10.2204/iodp.proc.309312.204.2009.

Nivia, A., 1996, The Bolivar mafic-ultramafic complex, SW Colombia: The base of an obducted oceanic plateau: Journal of South American Earth Sciences, v. 9, p. 59–68, doi:10.1016/0895-9811(96)00027-2.

Noël, J., Godard, M., Oliot, E., Martinez, I., Williams, M., Boudier, F., Rodriguez, O., Chaduteau, C., Escario, S., and Gouze, P., 2018, Evidence of polygenetic carbon trapping in the Oman Ophiolite: Petro-structural, geochemical, and carbon and oxygen isotope study of the Wadi Dima harzburgite-hosted carbonates (Wadi Tayin massif, Sultanate of Oman): Lithos, v. 323, p. 218–237, doi:10.1016/j.lithos.2018.08.020.

Okamoto, A., Nagaya, T., Endo, S., and Mizukami, T., 2024, Ultramafic Rocks from the Sanbagawa Belt: Records of Mantle Wedge Processes: Elements, v. 20, p. 83–88, doi:10.2138/gselements.20.2.83.

Okamoto, A., Oyanagi, R., Yoshida, K., Uno, M., Shimizu, H., and Satish-Kumar, M., 2021, Rupture of wet mantle wedge by self-promoting carbonation: Communications Earth & Environment, v. 2, p. 1–10, doi:10.1038/s43247-021-00224-5.

Oyanagi, R., and Okamoto, A., 2024, Subducted carbon weakens the forearc mantle wedge in a warm subduction zone: Nature Communications, v. 15, p. 7159, doi:10.1038/s41467-024-51476-6.

Oyanagi, R., Okamoto, A., Satish-Kumar, M., Minami, M., Harigane, Y., and Michibayashi, K., 2021, Hadal aragonite records venting of stagnant paleoseawater in the hydrated forearc mantle: Communications Earth & Environment, v. 2, p. 1–10, doi:10.1038/s43247-021-00317-1.

Oyanagi, R., Uno, M., and Okamoto, A., 2023, Metasomatism at a metapelite–ultramafic rock contact at the subduction interface: Insights into mass transfer and fluid flow at the mantle wedge corner: Contributions to Mineralogy and Petrology, v. 178, p. 27, doi:10.1007/s00410-023-02011-1.

Ozawa, H., Murata, M., Nishimura, H., and Itaya, T., 1997, Petrological Feature and Dating of Igneous Rocks of the Mikabu Belt: Bulletin of the Volcanological Society of Japan, v. 42, p. S231–S237, doi:10.18940/kazan.42.Special_S231.

Park, J., and Rye, D.M., 2019a, Broader Impacts of the Metasomatic Underplating Hypothesis: Geochemistry, Geophysics, Geosystems, v. 20, p. 4810–4829, doi:10.1029/2019GC008493.

Park, J., and Rye, D.M., 2019b, Why Is Crustal Underplating Beneath Many Hot Spot Islands Anisotropic? Geochemistry, Geophysics, Geosystems, v. 20, p. 4779–4809, doi:10.1029/2019GC008492.

Pearce, J.A., 2008, Geochemical fingerprinting of oceanic basalts with applications to ophiolite classification and the search for Archean oceanic crust: Lithos, v. 100, p. 14–48, doi:10.1016/j.lithos.2007.06.016.

Peng, W., Zhang, L., Menzel, M.D., Vitale Brovarone, A., Tumiati, S., Shen, T., and Hu, H., 2020, Multistage CO2 sequestration in the subduction zone: Insights from exhumed carbonated serpentinites, SW Tianshan UHP belt, China: Geochimica et Cosmochimica Acta, v. 270, p. 218–243, doi:10.1016/j.gca.2019.11.025.

Plank, T., 2014, The Chemical Composition of Subducting Sediments, *in* Treatise on Geochemistry, Elsevier, v. 4, p. 607–629, doi:10.1016/B978-0-08-095975-7.00319-3.

Plank, T., and Manning, C.E., 2019, Subducting carbon: Nature, v. 574, p. 343–352, doi:10.1038/s41586-019-1643-z.

Pourmand, A., Dauphas, N., and Ireland, T.J., 2012, A novel extraction chromatography and MC-ICP-MS technique for rapid analysis of REE, Sc and Y: Revising CI-chondrite and Post-Archean Australian Shale (PAAS) abundances: Chemical Geology, v. 291, p. 38–54, doi:10.1016/j.chemgeo.2011.08.011.

Richards, M., Contreras-Reyes, E., Lithgow-Bertelloni, C., Ghiorso, M., and Stixrude, L., 2013, Petrological interpretation of deep crustal intrusive bodies beneath oceanic hotspot provinces: Geochemistry, Geophysics, Geosystems, v. 14, p. 604–619, doi:10.1029/2012GC004448.

Ridley, V.A., and Richards, M.A., 2010, Deep crustal structure beneath large igneous provinces and the petrologic evolution of flood basalts: Geochemistry, Geophysics, Geosystems, v. 11, doi:10.1029/2009GC002935.

Ripperdan, R.L., 2001, Stratigraphic Variation in Marine Carbonate Carbon Isotope Ratios: Reviews in Mineralogy and Geochemistry, v. 43, p. 637–662, doi:10.2138/gsrmg.43.1.637.

Sager, W.W., Sano, T., and Geldmacher, J., 2016, Earth-Science Reviews Formation and evolution of Shatsky Rise oceanic plateau : Insights from IODP Expedition 324 and recent geophysical cruises: Earth Science Reviews, v. 159, p. 306–336, doi:10.1016/j.earscirev.2016.05.011.

Sakai, R., Kusakabe, M., Noto, M., and Ishii, T., 1990, Origin of waters responsible for serpentinization of the Izu-Ogasawara-Mariana forearc seamounts in view of hydrogen and oxygen isotope ratios: Earth and Planetary Science Letters, v. 100, p. 291–303, doi:10.1016/0012-821X(90)90192-Z.

Sakakibara, M., Hori, R.S., and Murakami, T., 1993, Evidence from radiolarian chert xenoliths for post-Early Jurassic volcanism of the Mikabu greenrocks, Okuki area, western Shikoku, Japan: The Journal of the Geological Society of Japan, v. 99, p. 831- 833_1, doi:10.5575/geosoc.99.831.

Sano, T., Shimizu, K., Ishikawa, A., Senda, R., Chang, Q., Kimura, J.I., Widdowson, M., and Sager, W.W., 2012, Variety and origin of magmas on Shatsky Rise, northwest Pacific Ocean: Geochemistry, Geophysics, Geosystems, v. 13, doi:10.1029/2012GC004235.

Sawada, H., Isozaki, Y., Aoki, S., Sakata, S., Sawaki, Y., Hasegawa, R., and Nakamura, Y., 2019, The Late Jurassic magmatic protoliths of the Mikabu greenstones in SW Japan: A fragment of an oceanic plateau in the Paleo-Pacific Ocean: Journal of Asian Earth Sciences, v. 169, p. 228–236, doi:10.1016/j.jseaes.2018.08.018.

Scambelluri, M., Bebout, G.E., Belmonte, D., Gilio, M., Campomenosi, N., Collins, N., and Crispini, L., 2016, Carbonation of subduction-zone serpentinite (high-pressure ophicarbonate; Ligurian Western Alps) and implications for the deep carbon cycling: Earth and Planetary Science Letters, v. 441, p. 155–166, doi:10.1016/j.epsl.2016.02.034.

Schaller, M.F., Wright, J.D., Kent, D. V., and Olsen, P.E., 2012, Rapid emplacement of the Central Atlantic Magmatic Province as a net sink for CO2: Earth and Planetary Science Letters, v. 323–324, p. 27–39, doi:10.1016/j.epsl.2011.12.028.

Schmidt, K., Koschinsky, A., Garbe-Schönberg, D., de Carvalho, L.M., and Seifert, R., 2007, Geochemistry of hydrothermal fluids from the ultramafic-hosted Logatchev hydrothermal field, 15°N on the Mid-Atlantic Ridge: Temporal and spatial investigation: Chemical Geology, v. 242, p. 1–21, doi:10.1016/j.chemgeo.2007.01.023.

Schwarzenbach, E.M., Gill, B.C., Gazel, E., and Madrigal, P., 2016, Sulfur and carbon geochemistry of the Santa Elena peridotites: Comparing oceanic and continental processes during peridotite alteration: Lithos, v. 252–253, p. 92–108, doi:10.1016/j.lithos.2016.02.017.

Seki, Y., and Kuriyagawa, S., 1961, Mafic and leucocratic rocks associated with serpentinite of Kanasaki, Kanto Mountains, central Japan: Japanese Journal of Geology and Geography, v. 33, p. 15–32.

Smrzka, D., Zwicker, J., Bach, W., Feng, D., Himmler, T., Chen, D., and Peckmann, J., 2019, The behavior of trace elements in seawater, sedimentary pore water, and their incorporation into carbonate minerals: a review: Facies, v. 65, p. 41, doi:10.1007/s10347-019-0581-4.

Suzuki, N., Saito, H., and Hoshino, T., 2017, Hydrogen gas of organic origin in shales and metapelites: International Journal of Coal Geology, v. 173, p. 227–236, doi:10.1016/j.coal.2017.02.014.

Takasu, A., and Dallmeyer, R.D., 1990, ^{40}Ar/^{39}Ar mineral age constraints for the tectonothermal evolution of the Sambagawa metamorphic belt, central Shikoku, Japan: a Cretaceous accretionary prism: Tectonophysics, v. 185, p. 111–139, doi:10.1016/0040-1951(90)90408-Z.

Tamura, A., and Arai, S., 2006, Harzburgite-dunite-orthopyroxenite suite as a record of supra-subduction zone setting for the Oman ophiolite mantle: Lithos, v. 90, p. 43–56, doi:10.1016/j.lithos.2005.12.012.

Tatsumi, Y., Shinjoe, H., Ishizuka, H., Sager, W.W., and Klaus, A., 1998, Geochemical evidence for a mid-Cretaceous superplume: Geology, v. 26, p. 151, doi:10.1130/0091-7613(1998)026<0151:GEFAMC>2.3.CO;2.

Tejada, M.L.G., Mahoney, J.J., Neal, C.R., Duncan, R.A., and Petterson, M.G., 2002, Basement Geochemistry and Geochronology of Central Malaita, Solomon Islands, with Implications for the Origin and Evolution of the Ontong Java Plateau: Journal of Petrology, v. 43, p. 449–484, doi:10.1093/petrology/43.3.449.

Ternieten, L., Früh-Green, G.L., and Bernasconi, S.M., 2021, Distribution and Sources of Carbon in Serpentinized Mantle Peridotites at the Atlantis Massif (IODP Expedition 357): Journal of Geophysical Research: Solid Earth, v. 126, doi:10.1029/2021JB021973.

Tetreault, J.L., and Buiter, S.J.H., 2014, Future accreted terranes: A compilation of island arcs, oceanic plateaus, submarine ridges, seamounts, and continental fragments: Solid Earth, v. 5, p. 1243–1275, doi:10.5194/se-5-1243-2014.

Tetreault, J.L., and Buiter, S.J.H., 2012, Geodynamic models of terrane accretion: Testing the fate of island arcs, oceanic plateaus, and continental fragments in subduction zones: Journal of Geophysical Research: Solid Earth, v. 117, p. 1–23, doi:10.1029/2012JB009316.

Tokuda, M., 1986, Mountains., Study on the Geological Structure of the Sambagawa-Chichibu Belts in the Kanto: Geological report of the Hiroshima University, v. 26, p. 260, doi:10.15027/52892.

Tominaga, K., and Hara, H., 2021, Paleogeography of Late Jurassic large-igneous-province activity in the Paleo-Pacific Ocean: Constraints from the Mikabu greenstones and Chichibu accretionary complex, Kanto Mountains, Central Japan: Gondwana Research, v. 89, p. 177–192, doi:10.1016/j.gr.2020.10.003.

Treves, B.E., and Harper, G.D., 1994, Exposure of serpentinites on the ocean floor: sequence of faulting and hydrofracturing in the Northern Apennine ophicalcites: Ofioliti, v. 19, p. 435–466.

Uesugi, J., and Arai, S., 1999, The Shiokawa peridotite mass in the Mikabu belt, central Japan, as a cumulate from intra-plate tholeiite: The Memoirs of the Geological Society of Japan, v. 52, p. 229–242.

Uno, M., Koyanagawa, K., Kasahara, H., Okamoto, A., and Tsuchiya, N., 2022, Volatile-consuming reactions fracture rocks and self-accelerate fluid flow in the lithosphere: Proceedings of the National Academy of Sciences, v. 119, p. e2110776118, doi:10.1073/pnas.2110776118.

Veizer, J., and Prokoph, A., 2015, Temperatures and oxygen isotopic composition of Phanerozoic oceans: Earth-Science Reviews, v. 146, p. 92–104, doi:10.1016/j.earscirev.2015.03.008.

Wallis, S., and Aoya, M., 2000, A re-evaluation of eclogite facies metamorphism in SW Japan: proposal for an eclogite nappe: Journal of Metamorphic Geology, v. 18, p. 653–664, doi:10.1046/j.1525-1314.2000.00285.x.

Wallis, S., Takasu, A., Enami, M., and Tsujimori, T., 2000, Eclogite and related metamorphism in the Sanbagawa belt, Southwest Japan: Bulletin of Research Institute of Natural Sciences, Okayama University of Science, v. 26, p. 3–17.

Wallis, S.R., Yamaoka, K., Mori, H., Ishiwatari, A., Miyazaki, K., and Ueda, H., 2020, The basement geology of Japan from A to Z: Island Arc, v. 29, doi:10.1111/iar.12339.

Wasilewski, B. et al., 2017, Ultra-refractory mantle within oceanic plateau: Petrology of the spinel harzburgites from Lac Michèle, Kerguelen Archipelago: Lithos, v. 272–273, p. 336–349, doi:10.1016/j.lithos.2016.12.010.

Xia, L., and Li, X., 2019, Basalt geochemistry as a diagnostic indicator of tectonic setting: Gondwana Research, v. 65, p. 43–67, doi:10.1016/j.gr.2018.08.006.

Yamaguchi, A., Ujiie, K., Nakai, S., and Kimura, G., 2012, Sources and physicochemical characteristics of fluids along a subduction-zone megathrust: A geochemical approach using syn-tectonic mineral veins in the Mugi mélange, Shimanto accretionary complex: Geochemistry, Geophysics, Geosystems, v. 13, doi:10.1029/2012GC004137.

Yoshida, K., Niki, S., Sawada, H., Oyanagi, R., Hirata, T., Asakura, K., and Hirajima, T., 2021, Discovery of the Early Jurassic high-temperature pre-Sanbagawa metamorphism recorded in titanite: Lithos, v. 398–399, p. 106349, doi:10.1016/j.lithos.2021.106349.

Yoshida, K., Okamoto, A., Shimizu, H., Oyanagi, R., and Tsuchiya, N., 2020, Fluid Infiltration Through Oceanic Lower Crust in Response to Reaction-Induced Fracturing: Insights From Serpentinized Troctolite and Numerical Models: Journal of Geophysical Research: Solid Earth, v. 125, doi:10.1029/2020JB020268.

Zhang, S., and DePaolo, D.J., 2020, Equilibrium calcite-fluid Sr/Ca partition coefficient from marine sediment and pore fluids: Geochimica et Cosmochimica Acta, v. 289, p. 33–46, doi:10.1016/j.gca.2020.08.017.

TABLE 1 THE SAMPLE LIST AND APPLIED CARBONATE ANALYSIS

Sample ID	Lithology	Carbonate	Carbonate occurrence	Carbonate geochemical analyses			
				C-O isotope*	Sr isotope	ICP-MS	LA-ICP-MS
KN220423	Bastite serpentinite	-	N.A.	N.A.	N.A.	N.A.	N.A.
KN22093001	Bastite serpentinite	-	N.A.	N.A.	N.A.	N.A.	N.A.
KN22093005	Bastite serpentinite	-	N.A.	N.A.	N.A.	N.A.	N.A.
KN22093006	Bastite serpentinite	-	N.A.	N.A.	N.A.	N.A.	N.A.
KN22093007	Bastite serpentinite	-	N.A.	N.A.	N.A.	N.A.	N.A.
KN22093008	Massive serpentinite	-	N.A.	N.A.	N.A.	N.A.	N.A.
KN22093013	Massive serpentinite	-	N.A.	N.A.	N.A.	N.A.	N.A.
KN22093015	Massive serpentinite	-	N.A.	N.A.	N.A.	N.A.	N.A.
KN22072501	Ophicarbonate	Cal	Type I	○ (6)	○	○	○
KN22093004	Ophicarbonate	Cal	Type I	○ (1)	○	○	N.D.
KN22093012	Ophicarbonate	Cal	Type I	○ (1)	○	○	N.D.
KN22093014	Ophicarbonate	Cal	Type I	○ (3)	○	○	○
KN23011002	Ophicarbonate	Cal	Type I	○ (1)	○	○	N.D.
KN23011003	Ophicarbonate	Cal	Type I	N.D.	N.D.	N.D.	N.D.
KN23011004	Ophicarbonate	Cal	Type I	N.D.	N.D.	N.D.	N.D.
KN23011005	Ophicarbonate	Cal	Type I	○ (1)	N.D.	N.D.	N.D.
KN23011006	Ophicarbonate	Cal	Type I	○ (1)	○	○	N.D.
KN23011007	Ophicarbonate	Cal	Type I	○ (1)	○	○	○
KN22093009	Ophicarbonate	Dol + cal	Type II	○ (1)	○	N.D.	N.D.
KN22093010	Ophicarbonate	Dol + cal	Type II	○ (1)	○	N.D.	○
KN22093011[†]	Ophicarbonate	Dol + cal	Type II	○ (4)	○	○	○
KN22072503	Ophicarbonate	Cal	Type III	○ (3)	○	○	○
KN23011101	Ophicarbonate	Cal	Type III	○ (1)	○	○	N.D.
KN22093011[†]	Ophicarbonate	Dol + cal	Type IV	○ (3)	○	○	○

Note: Cal = calcite; Dol = dolomite; N.A. = not applicable; N.D. = not determined.

[*] Number in the parentheses indicate the number of C-O analysis in a single sample.

[†] Two carbonate occurrences (type II and IV) in a single sample (KN22093011) were saparetely described.

TABLE 2. SUMMARY OF ISOTOPIC AND TRACE ELEMENTS COMPOSITION OF BULK CARBONATE

Sample ID	Carbonate type	$\delta^{13}C$ (‰ VPDB)	$\delta^{18}O$ (‰ VSMOW)	$^{87}Sr/^{86}Sr$ at prensent	$\pm 2\sigma \times 10^6$	$^{87}Sr/^{86}Sr$ at 150Ma	$^{87}Sr/^{86}Sr$ at 500Ma	Rb (mg kg^{-1})	Sr (mg kg^{-1})	Mn (mg kg^{-1})	U (mg kg^{-1})	Rb/Sr	Mn/Sr	Y/Ho	Ce/Ce*	Eu/Eu*	Pr_{SN}/Yb_{SN}
KN22072501	Type I	1.78[†]	14.58[†]	0.707036	14	0.707036	0.707035	0.01	270	793	0.007	5.6×10^{-5}	2.9	37	0.60	1.36	0.13
KN22093004	Type I	2.02	13.31	0.706883	14	0.706882	0.706881	0.04	392	230	0.058	1.1×10^{-4}	0.6	61	0.23	1.13	0.69
KN22093012	Type I	-0.99	15.08	0.706300	14	0.706300	0.706300	0.05	2616	1309	0.061	2.0×10^{-5}	0.5	39	0.71	2.61	0.32
KN22093014	Type I	-1.81[†]	14.62[†]	0.706312	14	0.706312	0.706312	0.01	3961	4337	b.d.l.	2.6×10^{-6}	1.1	37	0.96	13.09	1.89
KN23011002	Type I	1.58	15.69	0.707082	14	0.707079	0.707072	0.10	206	936	0.070	4.9×10^{-4}	4.5	51	0.67	2.54	0.33
KN23011005	Type I	-0.11	14.92	N.D.	N.D.	N.D.	N.D.	N.D.	N.D.	N.D.	N.D.	N.D.	N.D.	N.D.	N.D.	N.D.	N.D.
KN23011006	Type I	0.92	14.39	0.707675	14	0.707674	0.707671	0.06	293	1045	0.066	2.2×10^{-4}	3.6	40	0.71	3.66	0.24
KN23011007	Type I	0.64	15.71	0.707666	14	0.707666	0.707664	0.03	403	1366	0.037	7.9×10^{-5}	3.4	43	0.80	2.45	0.14
KN22093009	Type II	-7.53	19.22	0.708382	32	N.D.	N.D.	N.D.	N.D.	N.D.	N.D.	N.D.	N.D.	N.D.	N.D.	N.D.	N.D.
KN22093010	Type II	-6.88	14.71	0.708280	46	N.D.	N.D.	N.D.	N.D.	N.D.	N.D.	N.D.	N.D.	N.D.	N.D.	N.D.	N.D.
KN22093011	Type II	-7.47[†]	17.47[†]	0.708358	16	0.708358	0.708358	0.02	2462	6423	b.d.l.	1.0×10^{-5}	2.6	46	0.98	7.49	2.22
KN22072503	Type III	-5.85[†]	13.84	0.707477	14	0.707477	0.707477	0.00	516	6289	b.d.l.	8.8×10^{-6}	12.2	37	0.91	4.41	0.13
KN23011101	Type III	-8.07	16.29	0.707142	14	0.707142	0.707142	0.01	3144	4341	b.d.l.	4.0×10^{-6}	1.4	31	0.92	20.19	0.12
KN22093011	Type IV	-7.28[†]	16.14[†]	0.708351	14	0.708351	0.708351	0.01	4869	6279	b.d.l.	2.4×10^{-6}	1.3	39	0.92	7.84	0.78
Refrence materials for isotopic analyses																	
NBS-18	N.A.	-4.97±0.12 (-5.01)[§]	7.22±0.20 (7.19)[§]	N.A.	N.A.	N.A.	N.A.	N.A.	N.A.	N.A.	N.A.	N.A.	N.A.	N.A.	N.A.	N.A.	N.A.
NBS-20	N.A.	-1.03±0.09 (-1.06)[§]	26.22±0.29 (26.64)[§]	N.A.	N.A.	N.A.	N.A.	N.A.	N.A.	N.A.	N.A.	N.A.	N.A.	N.A.	N.A.	N.A.	N.A.
NIST 987	N.A.	N.A.	N.A.	0.710251 ± 0.000003 (0.710248)[§]	N.A.	N.A.	N.A.	N.A.	N.A.	N.A.	N.A.	N.A.	N.A.	N.A.	N.A.	N.A.	N.A.

Note: N.D. = not determined. N.A. = not applicable. b.d.l. = below detection limit. VPDB = Vienna Peedee Belemnite. VSMOW = Vienna Standard Mean Ocean Water. Comprehensive analytical results of bulk trace element, in-situ trace element, and C-O isotope were showed in the Table S1, S3, and S7, respectively.

[†] Multiple analytical results in a single sample were averaged.

[§] Number in the paranthesis is recommended values.